UNIVERSITY OF ZULULAND

INVESTIGATION OF $Co_{1-2x}Ni_xMn_xCe_yFe_{2-y}O_4$ DOUBLE-SUBSTITUTION SPINEL FOR HIGHLY EFFICIENT DETECTION OF FLAMMABLE AND HAZARDOUS LIQUEFIED PETROLEUM GAS: SENSING PERFORMANCE

SUNDAY AYODEJI OGUNDIPE

2022

UNIVERSITY OF ZULULAND

INVESTIGATION OF $Co_{1-2x}Ni_xMn_xCe_yFe_{2-y}O_4$ Double-Substitution Spinel FOR HIGHLY EFFICIENT DETECTION OF FLAMMABLE AND HAZARDOUS LIQUEFIED PETROLEUM GAS: SENSING PERFORMANCE

Dissertation submitted in partial fulfilment of the requirements for the degree of Master of Science in the:

Faculty of Science, Agriculture and Engineering

Physics department

Supervisor: Dr. S.S Nkosi

Co-supervisors: Prof N. Revaprasadu, Dr. C.L Ndlangamandla

Candidate:

Sunday Ayodeji Ogundipe

October 2022

DECLARATION

I, the undersigned, hereby declare that the work contained in this dissertation is my own original work and effort and that I have not in its entirety or in part submitted it at any university for a degree.

Signature: ……  …….

Date: …….12 August, 2022…….

ABSTRACT

The presence of high concentrations of flammable gases and volatile organic compounds in the atmosphere has recently been reported to be detrimental to human survival. A lot of research effort has been directed towards finding an efficient means of quick detection of these gases below their 'immediately dangerous to life or health' concentrations. Also, detecting these gases in an oxygen-deficient environment is a crucial task to consider. In this research, double substitution spinels with chemical formula $Co_{1-2x}Ni_xMn_xFe_{2-y}Ce_yO_4$, where $0 \leq x = y \leq 0.3$, were prepared via the glycol-thermal technique. The final products following the appropriate substitution were $CoFe_2O_4$ (dried naturally), $CoFe_2O_4$ (dried with Infrared lamp), $Co_{0.8}Ni_{0.1}Mn_{0.1}Fe_{1.9}Ce_{0.1}O_4$, $Co_{0.6}Ni_{0.2}Mn_{0.2}Fe_{1.8}Ce_{0.2}O_4$, and $Co_{0.8}Ni_{0.1}Mn_{0.1}Fe_{1.9}Ce_{0.1}O_4$ spinel ferrites. X-ray diffractometry (XRD), high resolution transmission electron micrographs (HRTEM), and X-ray photoelectron spectroscopy (XPS) of the samples confirm the formation of the spinels. The gas sensing performance of these samples was tested at an operating temperature of 225 ºC towards liquefied petroleum gas (LPG), ammonia, ethanol and propanol using nitrogen, argon, helium, and dry air, each at different times as carrier gases. The $Co_{0.8}Ni_{0.1}Mn_{0.1}Fe_{1.9}Ce_{0.1}O_4$-based sensor was selective to LPG, with a high response of 116.43 towards 0.6 vol % of LPG, using helium as carrier gas. The response and recovery times of this sensor were 2.68 minutes and 3.01 minutes respectively. The sensor proved to be a potential tool for LPG detection in an oxygen-deficient environment.

Keywords: LPG sensing, chemoresistive gas sensors, spinel, fluctuating operating temperature, carrier gas, current oscillation.

LIST OF ABBREVIATIONS

LEL	Lower Explosive Limit
IDLH	Immediately Dangerous to Life or Health
NIOSH	National Institute for Occupational Safety and Health
DC	Direct Current
RF	Radio Frequency
IR	Infrared
UV-Vis	Ultraviolet-visible spectroscopy
PL	Photoluminescence
XRD	X-Ray Diffraction
XPS	X-ray Photoelectron Spectroscopy
BET	Brunauer-Emmett-Teller
TGA	Thermogravimetric Analysis
SEM	Scanning Electron Microscopy
HRTEM	High Resolution Transmission Electron Microscopy
PDF	Powder diffraction File
SAED	Selected Area Electron Diffraction
LPG	Liquefied Petroleum Gas
VOC	Volatile Organic Compound
NH_3	Ammonia
NO_2	Nitrogen dioxide
CO	Carbon monoxide
SO_2	Sulphur dioxide
H_2S	Hydrogen sulphide
NO	Nitrogen monoxide
H_2	Nitric oxide
CO_2	Carbon dioxide
PANI	Polyaniline
PAH	Polyamide hydrazide
$CoCl_2.6H_2O$	Cobalt (II) chloride, hexahydrate
$NiCl_2.6H_2O$	Nickel (II) chloride, hexahydrate
$MnCl_2.4H_2O$	Manganese (II) chloride,tetrahydrate
$CeCl_3.7H_2O$	Cerium (III) chloride, heptahydrate
$FeCl_3.6H_2O$	Iron (III) chloride, hexahydrate
MOS	Metal-oxide semiconductor
ZnO	Zinc oxide
SnO_2	Tin oxide
TiO_2	Titanium oxide
WO_3	tungsten trioxide
CuO	Copper oxide
MoO_3	Molybdenum oxide
In_2O_3	Indium oxide

Ga_2O_3	Gadolinium oxide
NiO	Nickel oxide
Cr_2O_3	Chromium oxide
V_2O_5	Vanadium oxide
Co_3O_4	Cobalt oxide
Mn_3O_4	Manganese oxide
Fe_2O_3	Iron (III) Oxide
Au-NiO	Gold-doped Nickel oxide
Pd-WO_3	Palladium-doped tungsten trioxide
Au-WO_3	Gold-doped tungsten trioxide
$GdFeO_3$	Gadolinium ferrite
$LaFeO_3$	Lanthanum ferrite
$NdFeO_3$	Neodymium ferrite
$CoFe_2O_4$	Cobalt ferrite
$MgFe_2O_4$	Magnesium ferrite
$NiFe_2O_4$	Nickel ferrite
$CuFe_2O_4$	Copper ferrite
$ZnFe_2O_4$	Zinc ferrite
CeO_2	Cerium oxide

DEDICATION

To the King eternal, immortal and invisible God- who alone is wise.

ACKNOWLEDGEMENTS

My profound gratitude to the Most Excellent God for His perfect guidance and tremendous assistance from the beginning to the end of this work.

I sincerely appreciate the immense efforts, constant support and competent supervision of my supervisors, Dr. S. S. Nkosi, Prof. N. Revaprasadu and Dr. C. L Ndlangamandla.

I am grateful to Prof. T. P. Jili, whose kindness, words of encouragement and usual prompt response to my urgent needs contributed immeasurably to my focus on the research. I am also grateful to Mr. P.S Mkwae, Mr S. Khanyile, Mrs Ntombifuthi Mothapo and the entire physics department for every form of support received during this work.

Many thanks to my dear friend, Dr. Sunday Olaniran, for his immense support, encouragement, and guidance from the inception of my study at the University of Zululand. His unflinching insistence, gentle persuasion, and consistent supportive attitude made my pursuit of a higher degree a possibility.

Lastly, I acknowledge the crucial role of my mother, Mrs. Christianah Ogundipe and my siblings Ms Bamidele Ogundipe, Mr. Taiwo Ogundipe and Ms Kehinde Muibi: thank you for your prayers and support which proved tremendously effective towards achieving this goal.

TABLE OF CONTENTS

LIST OF TABLES

LIST OF FIGURES

CHAPTER 1

1. INTRODUCTION, BRIEF HISTORY AND MOTIVATION

1.1. Introduction

The universe is made of matter which exists in three states - solid, liquid, or gas. Solids are characterised by definite volume and shape, liquids have definite volume without definite shape - they assume the shape of their containing vessels, while gases have neither definite volume nor definite shape **[1]**. Owing to the weak intermolecular force of attraction in gases, they can flow easily through space. The surrounding atmosphere consists of oxygen, nitrogen and various other gases which support the safe existence of humans. However, the recent industrial revolution, together with other human activities has caused environmental pollution from the release of harmful gases into the atmosphere **[2]**. The release of these harmful gases is associated with certain environmental and medical conditions such as global warming, climate change, and respiratory diseases.

Over the past few decades, gas sensing has attracted a lot of attention due to increased concern about human health, global warming, environmental air quality control, and climate change. It is well known that when toxic gases such as ammonia (NH_3), nitrogen dioxide (NO_2), carbon monoxide (CO), sulphur dioxide (SO_2), hydrogen sulphide (H_2S), and liquefied petroleum gas (LPG) are present in high concentration in the air, the result is usually detrimental to human survival. Certain other gases known as greenhouse gases cause heat trapping in the lower atmosphere of the earth, resulting in global warming. Some other gases are highly flammable and require constant monitoring to ensure safe living and working conditions **[3]**.

In the year 2006, a group of 120 countries met to sign what is popularly known as the ‘Paris agreement’ as a measure to tackle the threat posed by indiscriminate emission

of air pollutant gases into the atmosphere **[4]**. Gas sensor fabrication is one of the measures that have been employed to check the detrimental impact of these toxic and highly flammable gases on the human environment. Casualties and loss of property are disasters that justify the necessity of fabricating highly sensitive, low-cost, and portable devices for real-time detection and monitoring of various harmful and flammable gases which adversely affect our environment **[5]**. The purpose of monitoring these gases is to aid in the immediate prevention of hazards in any event of gas leakage or silent escape of gas to the atmosphere **[3]**.

Liquefied petroleum gas (LPG) is a mixture of hydrocarbons in different proportions and is one of the toxic and highly flammable gases. Its constituent elements are propane (5-10%), butane (70-80%), methane, propylene, ethylene, and other hydrocarbons (1-5%) **[6, 7]**. LPG has a variety of applications - it is used in industry for heating furnaces, in agriculture for drying crops and flame weeding, in transportation as fuel for vehicles, in homes for cooking, and for electricity generation. Transportation, storage, and usage of LPG, however, requires a high degree of caution because of the associated high risk of explosion of the flammable gas **[8]**. The lower explosive limit (LEL) of LPG is 20, 000 ppm (2 vol%), which is the minimum concentration of this gas that can support its combustion in air. Also, its 'Immediately Dangerous to Life or Health (IDLH) concentration is 2, 000 ppm (0.2 vol%) as estimated by the National Institute for Occupational Safety and Health (NIOSH) **[8]**. This implies that sensing and monitoring of this very useful but hazardous gas should not be taken lightly. To guarantee safe use of this gas by its many users, highly efficient devices for quick detection of low concentrations of LPG are indispensable. In addition, exposure to high concentrations of LPG can result in various life-threatening conditions such as asphyxia, dizziness, suffocation, and death **[9, 10]**. In the quest to

forestall the risks associated with the use of LPG, a great deal of research has been carried out to discover more efficient sensor materials for its detection.

1.2. Types of gas sensors

There are different types of gas sensors. These are optical, acoustic-based, calorimetric, capacitance-based, electrochemical, and Metal Oxide-based gas sensors **[11-13]**. In optical sensors, there is a requirement for transparent materials (i.e., materials that allow passage of light through them) or materials whose luminous intensity varies with the surrounding conditions **[11]**. Their operation is based on luminescence quenching of an indicator such as fullerene, transition metal complex, organic dye, or polyamide-hydrazide (PAH). They have been successfully employed in testing the following gases: CO, CO_2, H_2, NO_2, H_2S, and NO while Au-NiO, Au-WO_3, Pd-WO_3, and Au-TiO_2 are some of the sensor materials employed **[11]**.

The operation of acoustic-based gas sensors is such that, when they are exposed to an analyte gas, there occurs a frequency shift of the surface acoustic wave in the gas's surrounding atmosphere. Usually, the passage of the surface acoustic waves through the sensing membrane of this sensor results in change in velocity of the transmitting wave owing to the interaction the wave and gas molecules. The sensitivity of this device to a target gas is defined by the difference between the frequency in pure air and the frequency in the presence of the target gas **[13]**.

In a calorimetric gas sensor, the outcome of the interaction between the gas molecules and the sensing surface is a temperature change. The sensor, thus, detects heat generated during the chemical reaction **[14, 15]**. The calorimetry-based sensors can be categorised into three, namely, adsorbent-based, catalytic, and thermal conductivity gas sensors, all of which operate using the same sensing mechanism

[15]. One disadvantage of this type of gas sensor is its operation at high temperatures which causes high energy consumption **[13]**.

The capacitive-based sensors respond to target gases by permitting the development of an electric field around them. When certain ceramics interact with gases such as CO and NO_2, they experience a change in permittivity. This property is useful in the design of capacitive sensors for detecting these gases. The change in permittivity can be detected as a change in the electrical capacitance of the device. **[16]**.

Electrochemical gas sensors are devices whose output is proportional to the partial pressure or the concentration of the gaseous species. They are classified into two groups, amperometric and potentiometric, depending on whether the output is an electric current or electromotive force. In an amperometric gas sensor, the current flowing through the system is directly related to the concentration of the target gas, whereas in the potentiometric gas sensor, the output produces an electromotive force, i.e., an open circuit voltage **[17]**. This sensor type is becoming outdated because of the shortness of its lifespan which makes it unsuitable for long-term monitoring.

Metal oxide semiconductor-based gas sensors have become popular for their low cost of fabrication, high sensitivity, long lifetime, small size, and short response time **[12]**. Their operation is based on chemoresistivity- the process by which the interaction between the sensing surface and the gaseous species results in change in the electrical resistance of the sensing element. The chemical reaction between the analyte gas and the sensing element takes place either on the surface of the sensing element or in the bulk of the material, resulting in a change in the electrical properties of the sensing material. With the aid of an appropriate transducer, this changed property can be transformed into an electrical signal **[12]**.

Gas sensors are required for a variety of purposes: safety - for detection of gas leakage which could lead to explosion and fire hazard, and as a breathalyser to prevent drunken driving; medical- to detect disease biomarkers for clinical diagnosis; agricultural - for food security **[14]**.

Several binary metal oxides have been extensively investigated for gas sensing applications. A survey of the literature indicates the exploration of such materials as ZnO, SnO_2, TiO_2, CuO, WO_3, MoO_3, In_2O_3, CeO_2, Ga_2O_3, NiO, Cr_2O_3, V_2O_5 etc., with high sensitivity towards various gases including ethanol, methanol, LPG, ammonia (NH_3), NO, NO_2, toluene, H_2S, and acetone **[2, 3, 18-20]**. However, some performance deficiency of these sensors with regard to LPG detection has, recently, prompted researchers to begin exploring ternary oxides for suitability in the selective detection of liquefied petroleum gas (LPG) **[8]**. Among the widely investigated ternary materials, spinel ferrites (AB_2O_4) have gained prominence. They possess excellent magnetic and electrical properties which make them suitable for many applications including electrical generators, drug delivery, photocatalysis, and gas sensing **[21, 22]**. In addition, they allow substitution in their structure, making them tunable and hence, widely used. These materials exhibit high gas sensitivity, and stability, and are operable at low temperatures. In general, the capability for: below lower explosive limit detection, low temperature operation, humidity-resistance and long-term stability is paramount, hence, the need for continued exploration of new materials for highly efficient devices to detect and monitor this highly flammable gas.

Considering the abovementioned reasons, this study investigated the double-substitution spinel for prospect in highly efficient detection of liquefied petroleum gas.

1.3. Problem statements

At its Lower Explosive Limit (LEL) (2 vol %), given the favourable condition, LPG will explode in the absence of naked flame, resulting in casualties and loss of property. If inhaled at higher concentrations, it will cause asphyxia, dizziness, and/or death. For safety purposes, the National Institute for Occupational Safety and Health (NIOSH) estimated that the 'Immediately Dangerous to Life or Health' (IDLH) concentration of LPG is 0.2 vol %.

For real time LPG detection and monitoring, a practical sensor must be operable at low temperatures with optimum performance. However, detecting LPG below its LEL and IDLH concentration with a low-temperature-operated device is still a challenge. Humidity is another factor that shortens the lifetime of a sensor and makes it inapplicable for long-term monitoring.

Therefore, there is a need for sensor materials that are highly sensitive to low concentrations of LPG at low operating temperatures and under different environmental conditions such as humid and oxygen-deficient environments.

1.4. Research aims and objectives

This study was aimed at investigating $Co_{1-2x}Ni_xMn_xCe_yFe_{2-y}O_4$ double-substitution spinel for highly efficient LPG sensing performance at low operating temperatures, in oxygen-deficient environments, for long-term monitoring and below IDLH concentration. In addition, we have recently observed that LPG sensing is often accompanied with fluctuation in operating temperature which consequently limits sensors' response. Therefore, it was part of this study to understand this anomaly for the fabrication of effective gas sensors to mitigate possible fatal threats under different ambient conditions. The following objectives were set to achieve the aim of the study:

i. synthesis of $Co_{1-2x}Ni_xMn_xCe_yFe_{2-y}O_4$ $(0 \leq x \leq 0.3)$

ii. structural and morphological characterisation of $Co_{1-2x}Ni_xMn_xCe_yFe_{2-y}O_4$ ($0 \leq x \leq 0.3$)

iii. fabrication of sensors

iv. detailed gas measurement and analysis of the sensors' performance.

1.5. Dissertation outline

Chapter 1: background discourse on gas sensors and gas sensing

Chapter 2: literature review on chemoresistive gas sensors

Chapter 3: characterisation techniques of powdery nanomaterials

Chapter 4: experimental details, results, and discussion

Chapter 5: conclusion and recommendation

References

[1]. R. Serway, J. Jewett. Physics for scientist and engineers with modern physics 9 (2014) 417.

[2]. L. Zhu, W. Zeng. Room temperature gas sensing of ZnO-based gas sensor: A review. Journal of Sensors and Actuators A 267 (2017) 242-261.

[3]. H. Ji, W. Zeng, Y. Li. Gas sensing mechanism of metal oxide semiconductors: A focus review. Journal of Nanoscale 11 (2019) 22664.

[4]. M. Nemufulwi, H. Swart, G. Mhlongo. A comprehensive comparison study on magnetic behaviour, defects-related emission and Ni substitution to clarify the origin of enhanced acetone detection capabilities. Journal of Sensors and Actuators: B. Chemical 339 (2021) 129860.

[5]. G. Manjunath, S. Pujaria, D. Patil, S. Mandala. A scalable screen-printed performance ZnO-UV and Gas Sensor: Effect of solution combustion. Journal of Materials Science in Semiconductor Processing 107 (2020) 104828.

[6]. M. Singh, B. Yadav, A. Ranjan, R. Sonker, M. Kaur. Detection of liquefied petroleum gas below lowest explosion limit (LEL) using nanostructured hexagonal strontium ferrite thin film. Journal of Sensors and Actuators B 249 (2017) 96 – 104.

[7]. S. Bagga, J. Akhtar, S. Mishra, Preeti. Fabrication of coplanar microheater platform for LPG sensing application. Springer Nature 26 (2019) 731-738.

[8]. V. Manikandan, M. Singh, B. Yadav, R. Mane, S. Vigneselvand, A. Mirzaei, J. Chandrasekaran. Room temperature LPG sensing properties of tin substituted copper ferrite (Sn-$CuFe_2O_4$) thin film. Journal of Materials Chemistry and Physics 240 (2020) 122265.

[9]. M. Reddy, S Kailasa· B. Rani· N. Jayarambabu · K. Bikshalu· P. Munindra · K. Rao. MgO@CeO2 chemiresistive fexible sensor for room temperature LPG detection. Journal of Materials Science 30 (2019) 17295–17302.

[10]. P. Munindra, M. Reddy, B. Rani, N. Jayarambabu, S. Kailasa, P. Rao, K. Rao. A high-performance low-temperature LPG detection by MgFe2O4/BiVO4 chemiresistive sensor. Journal of Materials Science: Materials in Electronics 31 (2020) 2370-2377.

[11]. G. Korotcenkov. Handbook of Gas Sensor Materials: Properties, Advantages and Shortcomings for Application: New Trends and Technologies, Integrated Analytical Systems 1 (2014) 167-195.

[12]. G. Neri. First fifty years of chemoresistive gas sensors. Journal of Chemosensors 3 (2015) 1-20.

[13]. H. Nazemi, A. Joseph, J. Park, A. Emadi. Advanced micro- and nano-gas sensor technology: A review. Journal of Sensors 19 (2019) 1285.

[14]. M. Fleischer, M. Lehmann. Solid state gas sensors- Industrial application: Springer series on chemical sensors and biosensors 11 (2012) 53-78.

[15]. C. Kohl, T. Wagner. Gas sensing fundamentals: Springer series on chemical sensors and biosensors 15 (2014) 279-310.

[16]. S. Zhao, W. Ran, D. Wang, R. Yin, Y. Yan, K.Jiang, Z. Lou, G. Shen. 3D dielectric layer enabled highly sensitive capacitive pressure sensors for wearable electronics. Journal of Applied Materials Interfaces 28 (2020) 32023-32030.

[17]. G. Sberveglieri. Gas Sensors: principles, operation, developments. Springer 1 (1992) 329-364.

[18]. P. Karnati, S. Akbar, P. Morris. Conduction mechanisms in one dimensional core-shell nanostructures for gas sensing: A review. Journal of Sensors and Actuators: B. Chemical 295 (2019) 127-143.

[19]. Z. Yuan, R. Li, F. Meng, J. Zhang, K. Zuo, E. Han. Approaches to Enhancing Gas Sensing Properties: A Review. Journal of Sensors 19 (2019) 1495.

[20]. Y. Wong, B. Ang, A. Haseeb, A. Baharuddin, Y. Wong. Conducting Polymers as Chemiresistive Gas Sensing Materials: A Review. Journal of The Electrochemical Society, 167 (2020) 037503.

[21]. A. Mugutka, S. Gore, R. Mane, S. Patang, S. Jadhav, S. Shaikh, A. Al-Enizi, A. Nafady, B. Thamer, M. Ubaidullah. Structural modifications in Co-Zn nanoferrites by Gd substitution triggering to dielectric and gas sensing applications. Journal of Alloys and Compounds 844 (2020) 156178.

[22]. M. Hashim, M. Raghashuda, S. Meena, J. Shah, S. Shirsath, S. Kumar, D. Ravinder, P. Bhatt, Alimuddin, R. kumar, R. Kotnala. Influence of rare earth ion doping (Ce and Dy) on electrical and magnetic properties of cobalt ferrite. Journal of Magnetism and Magnetic Materials 449 (2018) 319-327.

CHAPTER 2

2. LITERATURE REVIEW

2.1. Chemoresistive gas sensor

Materials for gas sensing are numerous and diverse. They include carbon-based nanostructures, nanofibers, metal oxide-based nanostructures, metal-based nanostructures, and semiconductor nanostructures, to mention a few. Each of these materials has its deficiencies with respect to sensing performance, and so cannot meet all the requirements for a highly efficient sensor. This is the reason for continued research to discover new sensor materials with suitable properties for the development of gas sensors with excellent functional characteristics **[1]**. Recently, metal oxide semiconductor-based gas sensors have attracted research interest with respect to gas sensing, owing to their large number of surface sites which facilitates reaction on the sensor surface. The metal-oxide nanostructures for gas sensing exhibit various surface morphologies such as nanowires, nanorods, nanotubes, nanoparticles, nanoflakes, nanoflowers, nanosheets, nanowalls, nanofibers, and nanosphere **[1-6]**. This difference in morphology could be due to processing conditions the starting materials are subjected to, the solvent used, or the synthesis method. Furthermore, they are classified as 0-D, 1-D, 2-D, and 3-D depending on their dimensionality **[3]**. In this study, the research was focused on 2-D nanomaterials (thin films) owing to their simplicity of operation and fabrication, low cost, low power consumption, and reusability. In general, metal-oxide semiconductor (MOS) materials for gas sensing may be either p-type or n-type depending on the majority charge carrier- holes in p-type materials, and electrons in n-type materials **[7]**. The response signal of an n-type material (e.g. SnO_2, $CoFe_2O_4$, ZnO, TiO_2, $MgFe_2O_4$, WO_3, Fe_2O_3, In_2O_3) on interaction with a reducing gas is always different

from that when an oxidising gas is under test. The same principle holds conversely for a p-type material such as NiO, Mn_3O_4, CuO, Co_3O_4. When a reducing gas reacts with n-type material, the current increases while the resistance decreases. If the same material is exposed to an oxidising material, the current decreases while the resistance of the material increases. Figure 2.1 shows the conductivity pattern for the n-type and p-type MOS gas sensors towards a reducing gas.

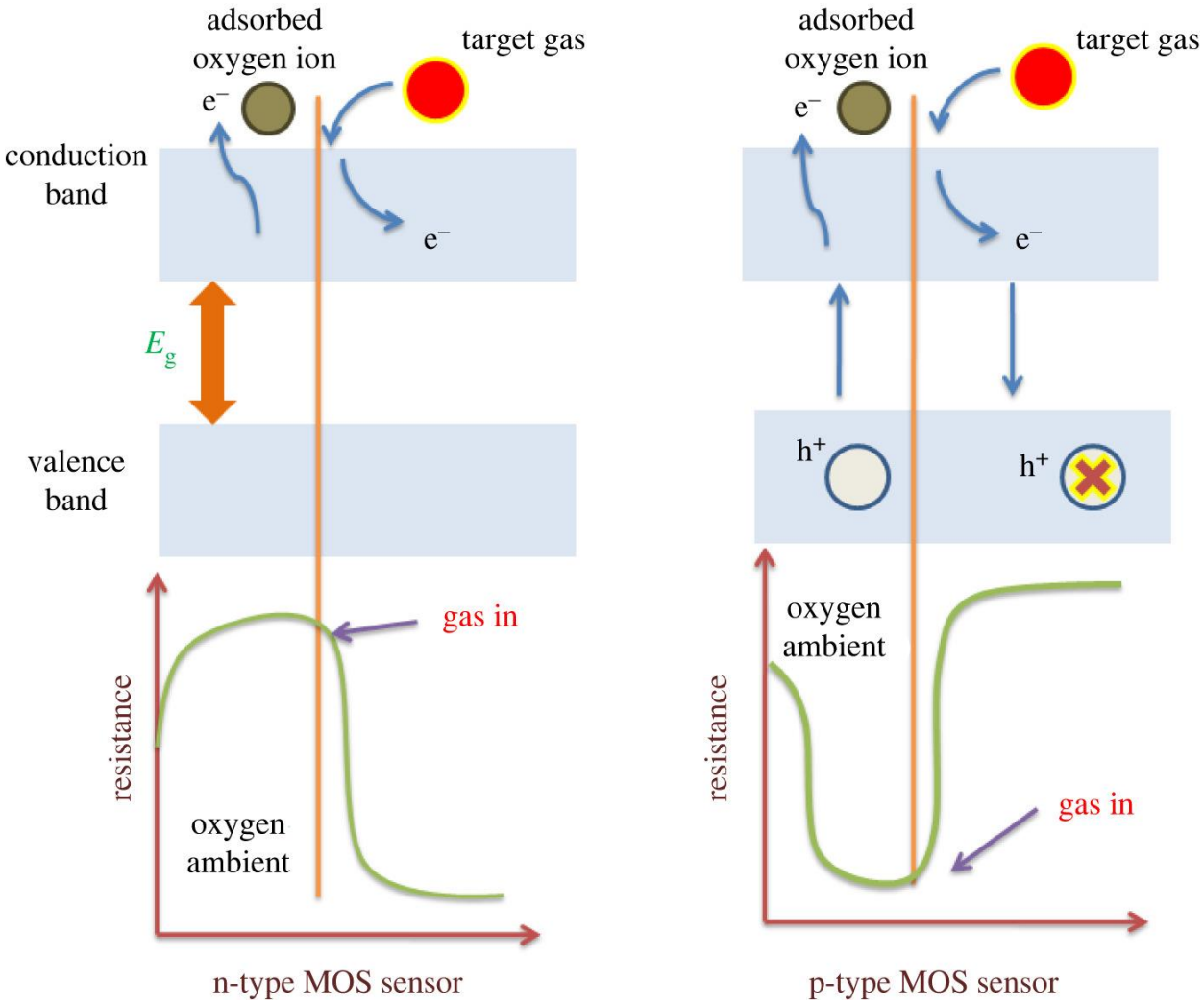

Figure 2.1. Conductivity pattern of n- and p-type MOS-based sensors towards a reducing gas **[8]**.

As depicted in figure 2.1, the resistivity of the n-type sensor decreases when exposed to the gas. The pattern is reversed when the chemical reaction takes place between the gas and a p-type sensor.

As mentioned in chapter 1, certain binary metal oxide semiconductors have been explored for gas sensing application and exhibited high sensitivity. However, they are deficient with regard to response time and selectivity. Perovskites are composites materials recently explored for gas sensing purposes. They have cubic structure and general formula ABO_3. The following are some of the perovskites that have been studied for gas sensing applications: $GdFeO_3$, $LaFeO_3$, $NdFeO_3$, and $SmFeO_3$. The excellent properties exhibited by perovskites make them relevant in different applications including, agriculture, biomedicine, industrial catalysis, environmental control, and gas sensing **[9]**.

Spinel, a class of minerals with the general formula AB_2X_4 possess cubic crystal structure with X anions (typically oxygen or sulphur) arranged in a cubic close-packed-lattice, while the cations A and B occupy the octahedral and tetrahedral lattice sites partly or in full. Cobalt spinel, chromium spinel, vanadium spinel, iron spinel, and aluminium spinel constitute the spinel group members. Currently, for gas sensing purpose, the most widely investigated of these is iron spinel. Iron spinel, more popularly known as spinel ferrite with the general formula $(M^{2+})[Fe^{3+}]_2O_4$ has a variety of applications, such as gas sensing, photocatalysis, hyperthermia, fuel cells, batteries technology, and hydrogen storage **[10]**. They are found to be very good materials for gas detection. A few of the spinel ferrites that have been commonly studied for application in gas sensing are: $MgFe_2O_4$ **[11]**, $NiFe_2O_4$ **[12]**, $CuFe_2O_4$ **[13]** and $ZnFe_2O_4$ **[14]**. These materials are excellent for their tolerance for substitution in their structures. A-site, B-site, or both sites' cations **[15-17]** can be

substituted with moderate amounts of dopant. This substitution usually influences their gas sensing properties or performance.

2.1.1. Methods of preparing chemoresistive nanostructures

The Figure 2.2 below exhibits the synthesis methods of chemoresistive nanomaterials.

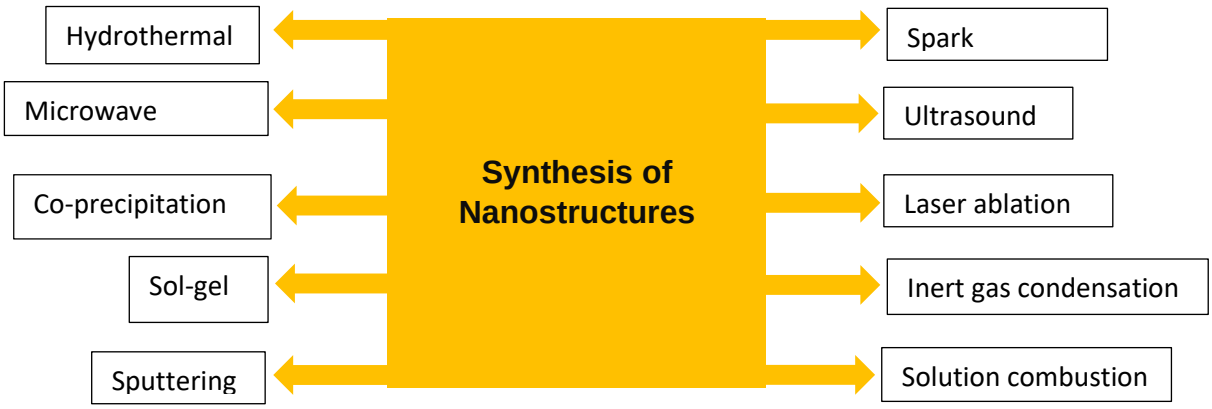

Figure 2.2. Methods of preparation of chemoresistive nanostructures.

The hydrothermal method is a sample preparation technique that involves the chemical reactions of substances heated above ambient temperature and pressure in a sealed solution. Crystal growth takes place in an autoclave (a stainless-steel pressure vessel). The formation of single crystals by hydrothermal process depends on the solubility of a substance in hot water at high pressure **[18]**. The hydrothermal synthesis technique is simple, scalable, cheap, compatible with a flexible substrate and requires low reaction temperatures **[3]**. However, it is impossible to monitor the reaction.

Microwave assisted method: chemical reactions are usually faster in microwave-assisted synthesis than in conventional heating. It is characterised by higher yield and fewer by-products. Heating occurs when the dipoles of irradiated molecules in solution try to align with the oscillating magnetic field. The movement and collision of ions in the oscillating field lead to the generation of more heat **[19]**.

Co-precipitation method: in this technique, nucleation, growth and/or agglomeration processes occur simultaneously. It is a simple, rapid processing method, that requires low temperature, but the challenge with this method is that trace impurities may precipitate with the product. Also, production is only batch by batch **[18]**.

Sol-gel method: in the sol-gel technique, the solution gradually evolves into a gel-like diphasic system containing solid and liquid phases. The precursors generally undergo the following process to form nanoparticles: dissolution, hydrolysis, poly-condensation, and aging. The products of this technique have high purity, but the process is time-consuming **[18]**.

Sputtering technique: sputtering refers to a process whereby atoms are ejected from the surface of a material (the target) by bombarding it with energetic particles. Sputtered atoms travel until they strike a substrate on which they form the desired layer. There are different methods of sputtering, namely; DC sputtering, magnetron sputtering, RF sputtering, and reactive sputtering. Almost all material types can be sputtered, making this method very advantageous although very expensive **[18]**.

Spark discharge: this process begins with the breakdown of a gas and the formation of a conducting channel. The gas molecules dissociate and ionize very quickly. The plasma (ionized gas) channel then expands, giving rise to shock wave generation. Eventually, charge carriers recombine, and as plasma cools, shock wave is attenuated to a sound wave while a high concentration of very small particles is formed **[20]**. The spark discharge technique is characterised by the following: synthesis of very small nanoparticles, low production rate, low impurity content of the synthesized nanoparticles, and relative simplicity of implementation **[18]**.

Ultrasound method: ultrasonic irradiation of liquids results in cavitation. Ultrasonic cavitation produces physical and chemical conditions for a chemical reaction to occur

under extreme conditions. It allows synthesis at ambient conditions but does not allow scale-up **[18]**.

Laser ablation: vapour, plasma, and metal micro- or nanosized droplets can be generated when a laser beam hits a metal target. A further reaction then occurs within the liquid medium to form nanoparticles. The main formation mechanisms of nanostructures by laser ablation are based on thermal evaporation and subsequent interaction with the liquid medium **[21]**.

Inert gas condensation: evaporation of material occurs at ultrahigh vacuum in a chamber filled with inert gas (helium or argon). The evaporated metal atoms then condense into small particles by losing their kinetic energy on collision with the gas. The small particles then grow by coagulating and coalescing into nanocrystals. This technique allows the control of particle size **[18]**.

Solution combustion: solution combustion synthesis involves a self-sustained redox exothermic reaction between hydrated metal nitrates and fuel (e.g. citric acid, urea, or glycine) mixed on a molecular level, which obeys all features of other combustible systems. The fuel provides sufficient heat for the system as well as ensuring formation of stable complexes with the metal ions to increase their solubility and prevent selective precipitation of the metal ions during water removal **[22]**.

Glycol-thermal: this technique is almost similar to the hydrothermal technique. The difference is that, while distilled water is the solvent for the reaction in the hydrothermal method, ethylene-glycol is the reaction solvent in the glycol-thermal method. It is suitable when the reaction temperature far exceeds the boiling point of water. When any other solvents than water or glycols are used, the preferred term for this method is solvothermal **[23]**.

2.1.2. Parameters of chemoresistive gas sensors

Chemoresistive gas sensors have many parameters, including, sensitivity/response, selectivity, reproducibility/repeatability, stability, response time, recovery time, lower detection limit, and thermal and chemical stability.

i. Sensitivity: The sensitivity or response of a sensor is its ability to react observably in the presence of a target gas. Response, S of a sensor is given by,

$$S = \frac{R_a}{R_g} \quad \text{or} \quad S = \frac{R_g}{R_a} \tag{2.1}$$

depending on the sensor material type and the nature of the gas (These determine the orientation of the resulting electrical signal).

R_g and R_a are resistances in the sensor circuit in the presence of gaseous species and in air, respectively.

ii. Selectivity: A good sensor should be able to respond more favourably to a particular gas in the presence of some other gases. This property of the gas sensor which enables it to single out one specific gas among some others is termed ‘selectivity’.

iii. Reproducibility: A sensor is said to be reproducible if it produces consistent output when tested over several cycles of the same concentration of gas.

iv. Stability: To consider a sensor for long-term monitoring, there should be observed, if ever there exists, an insignificant variation in response when continually used over a period of time.

v. Response time: Response time is the time taken for the sensor to attain 90% of the maximum current or resistance of the sensing film when exposed to a gas **[24].**

vi. Recovery time: The recovery time is the length of time required by the sensor to return approximately to its initial stage when the gas is off **[24]**.

vii. Lower detection limit: The minimum concentration (in ppm or vol%) of target gas that a sensor can distinguish from its complete absence in the air.

viii. Reversibility: ability of the sensor to return to its original condition after chemical reaction with gaseous species.

2.1.3. Factors affecting sensing performance of sensor materials

The performance of a semiconductor metal oxide-based gas sensor is influenced by certain conditions such as specific surface area, grain size, porosity, the density of defect, operating temperature, surface morphology, substitution, crystal structure and chemical composition.

i. Specific surface area: The effective specific area refers to the surface area of the sensing material available for interaction with the target gas. It influences the sensing performance of a sensor. The improved sensing performance of nickel-substituted cobalt ferrite sensor, with an increase in surface area, has been observed **[25]**. In general, the larger the surface area, the larger the available active sites for interaction with gas and the better the sensing performance.

ii. Grain size: Grains are tiny particles of the sensing material. The smaller the grain size the better the performance of a gas sensor.

iii. Porosity: The presence of pores on the surface of sensing materials facilitates adsorption on the sensing surface and, as a result, improves sensitivity.

iv. Density of defects: This may reduce sensitivity or increase it. It has been found in some cases that the introduction of defects to a pristine material enhances its performance, while in other instances increasing the amount of defect may lower the performance.

v. Operating temperature: Some materials perform excellently at elevated operating temperatures while others only require lower temperatures for optimum performance.

vi. Surface morphology: Altered surface morphology can imply the suitability of transition metal oxide for gas sensing purposes **[26]**. This shows the influence of surface structure and shape on gas sensing properties.

vii. Substitution: Introduction of foreign material has proven to significantly affect sensing performance.

viii. Crystal structure: The arrangement of atoms in the sensing crystallite also plays an important role in the sensing performance of metal oxide-based sensors.

ix. Chemical composition: the number of constituent elements of the sensing material is also an important factor.

2.1.4. Gas sensing mechanism of chemoresistive sensors

Metal oxide semiconductor-based sensors operate on the principle of chemoresistivity, i.e., change in electrical conductivity or resistivity of thin films on exposure to analyte gas. In air, at a particular temperature, atmospheric oxygen gets adsorbed on the sensing surface of a chemoresistive sensor, capturing electrons in the conduction band, thus changing the resistance of the sensor. Equations 2.2-2.5 demonstrate the oxygen species formation resulting from oxygen chemisorption on a sensor surface at different operating temperatures.

$$O_2(gas) \rightarrow O_2(ads) \qquad (2.2)$$

$$O_2(ads) + e^- \rightarrow O_2^-(ads) \qquad T < 100\,℃ \qquad (2.3)$$

$$O_2^-(ads) + e^- \rightarrow 2O^-(ads) \qquad 100\,℃ < T < 300\,℃ \qquad (2.4)$$

$$O^-(ads) + e^- \rightarrow O^{2-}(ads) \qquad T > 300\,℃ \qquad (2.5)$$ **[7]**.

On exposure of the sensor to analyte gas, the gas molecules Interact with the sensing surface and act as either electron donors or acceptors **[27, 28]**. A reducing gas reacts with chemisorbed oxygen species and causes the release of captured electrons back to the conduction band, thereby increasing the conductivity of an n-type sensor (because the majority carrier of n-type materials is electron). If the analyte gas is an oxidising type, its reaction with an n-type sensor will lead to increased resistivity as more electrons in the conduction band will be captured by further adsorption of oxygen on the sensor surface. Conversely, the interaction of a reducing gas with a p-type sensor will result in increased resistivity of the sensor system (the majority carrier of a p-type sensor material is hole, reducing gas interaction will lead to an increase of electrons in the conduction band resulting in depletion of the majority carrier), while the conductivity of the sensor will increase for p-type sensor/oxidising gas interaction. Figure 2.3 depicts the sensing mechanism of a metal-oxide based gas sensor.

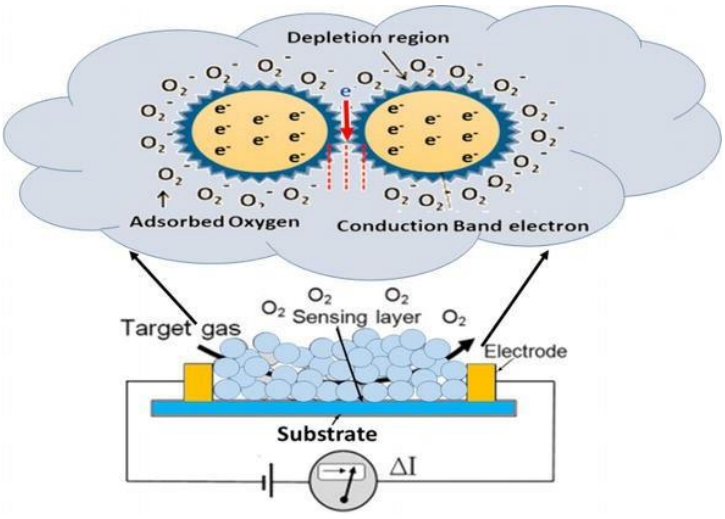

Figure 2.3. Sensing mechanism of a semiconducting metal oxide thin film gas sensor **[28]**.

2.2. A summary of recent work on LPG sensing

Figures 2.4(a-b) represents a summary of some recent works on LPG sensing. From the data presented, it is conclusive that there are not many good LPG sensors for practical applications, especially for use as a portable device. The $CoSm_{0.1}Fe_{1.9}O_4$ based sensor responded substantially to LPG with the response of 732 towards 10,000 ppm, except for its high operating temperature, long response, and recovery times. The TiO-ZnO-PANI based sensor, possesses an excellent sensing performance, with significant response towards low concentration of LPG at room temperature. However, an improvement in its response and recovery times is required.

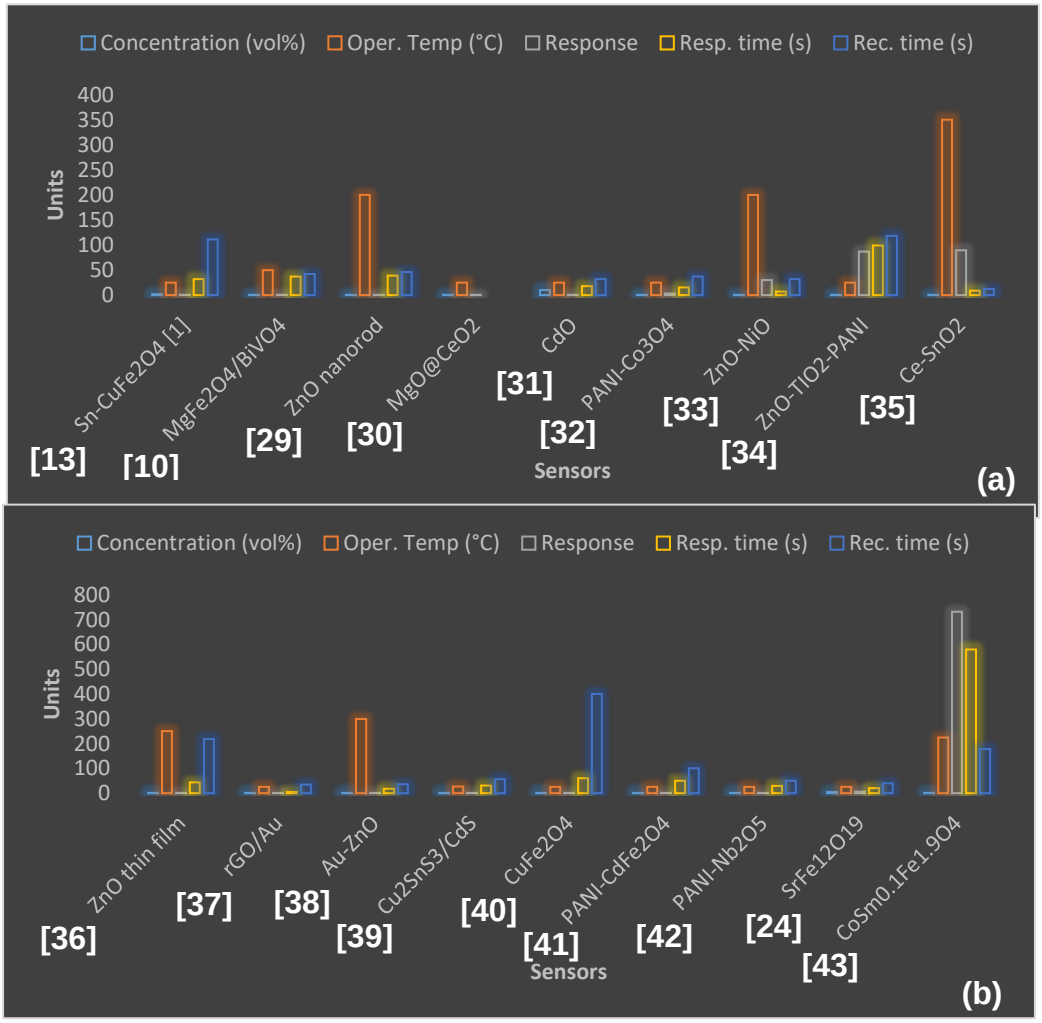

Figure 2.4. Pictorial representation of some recent work on LPG sensing.

2.3. The spinel and its gas sensing application

The spinels are known for excellent electrical properties which makes them suitable for various applications including gas sensing **[15, 17]**. The nanostructured spinel ferrites possess the general molecular formula $(A^{2+})[B_2^{3+}]O_4^{2-}$, where the divalent cation, A occupies the tetrahedral site, and the trivalent cation, B occupies the octahedral site **[44]**. A very important characteristic of the spinel is the ability to allow substitution in their structure, which is the principal means of improving the sensitivity and selectivity of gas sensors **[45]**. Of the spinel ferrite, cobalt-based ferrite exhibits interesting performance and has attracted researchers' attention in the gas sensing field **[17]**.

In view of the excellent performance of cobalt-based spinel and bearing in mind the need for a highly efficient LPG sensor, this work was undertaken to investigate $Co_{1-2x}Ni_xMn_xCe_yFe_{2-y}O_4$, which is a double substitution spinel, with expectation for high-performance marketable LPG sensor.

References

[1]. G. Korotcenkov. Handbook of Gas Sensor Materials: Properties, Advantages and Shortcomings for Application: New Trends and Technologies, Integrated Analytical Systems 1 (2014) 167-195.

[2]. D. Miller, S. Akbar, P. Morris. Nanoscale metal oxidebased heterojunctions for gas sensing: A review. Journal of Sensors and Actuators B 204 (2014) 250-272.

[3]. A. Dral, J. Elshof. 2D metal oxide nanoflakes for sensing applications: Review and perspective. Journal of Sensors and Actuators: B. Chemical 272 (2018) 369-392.

[4]. Z. Yuan, R. Li, F. Meng, J. Zhang, K. Zuo, E. Han. Approaches to Enhancing Gas Sensing Properties: A Review. Journal of Sensors 19 (2019) 1495.

[5]. L. Zhu, W. Zeng. Room temperature gas sensing of ZnO-based gas sensor: A Review. Journal of Sensors and Actuators A 267 (2017) 242-261.

[6]. Z. Li, H. Li, Z. Wu, M. Wang, J. Luo, H. Torun, P. Hu, C. Yang, M. Grundmann, X. Liud, Y. Fu. Advances in designs and mechanisms of semiconducting metal oxide nanostructures for high-precision gas sensors operated at room temperature. Journal of Materials Horizons 6 (2019) 470.

[7]. Y. Ding, X. Guo, B. Du, X. Hu, X. Yang, Y. He, Y. Zhou, Z. Zang. Low-operating temperature ammonia sensor based on Cu_2O nanoparticles decorated with p-type MoS_2 nanosheets. Journal of Materials Chemistry C 9 (2021) 4838-4846.

[8]. Y. Gautam, K. Sharma, S. Tyagi, A. Ambedkar, M. Chaudhary, B. Singh. Nanostructured metal oxide semiconductor-based sensors for greenhouse gas detection: progress and challenges. Journal of Royal Society Open Science 8 (2021) 201324.

[9]. Z. Anajafi, M. Naseri, G. Neria. Gas sensing and electrochemical properties of rare earth ferrite $LnFeO_3$ (Nd, Sm). Journal of Ceramics International 46 (2020) 26682-26688.

[10]. P. Munindra, M. Reddy, B. Rani, N. Jayarambabu, S Kailasa, P. Srinivasa, R. Venkateswara. A high-performance low-temperature LPG detection by $MgFe_2O_4/BiVO_4$ Chemiresistive sensor. Journal of materials Science: Materials in Electronics 31 (2020) 2370-2377.

[11]. J. Patil, D. Nadargi, I. Mulla, S. Suryavanshi. Spinel $MgFe_2O_4$ thick films: A colloidal approach for developing gas sensors. Journal of Materials Letters 213 (2018) 27-30.

[12]. P. Koli, K. Kapadnis, U. Deshpandhe. Nanocrystalline-modified nickel ferrite films: an effective sensor for industrial and environmental gas pollutant detection. Journal of nanostructure in chemistry 9 (2019) 95-110.

[13]. V. Manikandan, M. Singh, B. Yadav, R. Mane, S. Vigneselvand, A. Mirzaei, J. Chandrasekaran. Room temperature LPG sensing properties of tin substituted copper ferrite (Sn-$CuFe_2O_4$) thin film. Journal of Materials Chemistry and Physics 240 (2020) 122265.

[14]. M. Nemufulwi, H. Swart, G. Mhlongo. A comprehensive comparison study on magnetic behaviour, defects-related emission and Ni substitution to clarify the origin of enhanced acetone detection capabilities. Journal of Sensors and Actuators: B. Chemical 339 (2021) 129860.

[15]. M. Almesiere, Y. Silmani, A. Baykal. Synthesis and characterization of $Co_{1-2x}Ni_xMn_xCe_yFe_{2-y}O_4$ nanoparticles. Journal of Rare Earth 38 (2020) 188-194.

[16]. T. Roman, D. Gherca, A. Borhan, M. Grigoas, G. Stoian, N. Lupu, I. Turcan, N. Cimpoesu, B. Istrate, I. Radu, R. Danila, A. Pui. Nanostructured quaternary Ni_{1-}

$_xCu_xFe_{2-y}Ce_yO_4$ complex system: Cerium content and copper substitution dependence of cation distribution and magnetic-electric properties in spine ferrites. Journal of Ceramic International 47 (2021) 18177-18187.

[17]. A. Mugutka, S. Gore, R. Mane, S. Patang, S. Jadhav, S. Shaikh, A. Al-Enizi, A. Nafady, B. Thamer, M. Ubaidullah. Structural modifications in Co-Zn nanoferrites by Gd substitution triggering to dielectric and gas sensing applications. Journal of Alloys and Compounds 844 (2020) 156178.

[18]. A. Rane, K. kanny, V. Abitha, S. Thomas. Methods for synthesis of nanoparticles and fabrication of nanocomposites. Journal of Synthesis of inorganic materials: Advances and key technologies, Micro and Nano Technologies 5 (2018) 121-139.

[19]. V. Chikan, E. McLaurin. Rapid nanoparticle synthesis by magnetic and microwave heating. Journal of Nanomaterials 6 (2016) 85.

[20]. N. Tabrizi, M. Ullmann, V. Vons, U. Lafont, A. Schmidt-Ott. Generation of nanoparticles by spark discharge. Journal of Nanoparticles Research 11 (2009) 315–332.

[21]. H. Zeng, X. Du, S. Singh, S. Kulinich, S. Yang, J. He, W. Cai. Nanomaterials via Laser Ablation/Irradiation in Liquid: A Review. Journal of Advance Functional Materials 22 (2012) 1333–1353.

[22]. A. Varma, A. Mukasyan, A. Rogachev, K. Manukyan. Solution Combustion Synthesis of Nanoscale Materials. Journal of Chemical Reviews 116 (2016) 14493−14586.

[23]. A. Phuruangrat, S. Thongtem, T. Thongtem. Glycolthermal synthesis and characterization of hexagonal CdS round microparticles in flower-like clusters. Journal of Alloys and Compounds 509 (2011) 10150-10154.

[24]. M. Singh, B. Yadav, A. Ranjan, R. Sonker, M. Kaur. Detection of liquefied petroleum gas below lowest explosion limit (LEL) using nanostructured hexagonal strontium ferrite thin film. Journal of Sensors and Actuators B 249 (2017) 96 – 104.

[25]. Y. Zou, H. Wang, R. Yang, X. Lai, J. Wan, G. Lin, D. Liu. Controlled synthesis and enhanced toluene-sensing properties of mesoporous $NiCo_{1-x}Fe_2O_4$ nanostructured microspheres with tunable composite. Journal of Sensors and Actuators: B. chemical 280 (2019) 227-234.

[26]. S. Mutkule, S. Nayale, V. Jadhav, S. Ambade, M. Naushad, A. Sagar, V. Patil, F. Standler, R. Mane. Solution-processed nickel oxide films and their liquefied petroleum gas sensing activity. Journal of Alloys and Compounds 689 (2017) 2008-2015.

[27]. P. Shankar, J. Rayappan. Gas sensing mechanism of metal oxide: The role of ambient atmosphere, type of semiconductor and gases- A review. Journal of Science Letters 4 (2015) 126.

[28]. H. Ji, W. Zeng, and Y. Li. Gas sensing mechanisms of metal oxide semiconductor: A focus review. Journal of Nanoscale 11 (2019) 22664-22684.

[29]. S. Choudharya, S. Annapoorni, R. Malik. Evolution and growth mechanism of hexagonal ZnO nanorods and their LPG sensing response at low operating temperature. Journal of Sensors and Actuators 293 (2019) 201-214.

[30]. M. Reddy, S. Kailasa, B. Rani, N. Jayarambabu, K. Bikshalu, P. Munindra, K. Rao. MgO@CeO2 chemiresistive fexible sensor for room temperature LPG detection. Journal of Materials Science: Journal of Materials in Electronics (2019) 30:17295–17302.

[31]. U. Nakate, P. Patil, B. Ghule, Y. Nakate, S. Ekar, Revan C. Ambare, R.S. Mane. Room temperature LPG sensing properties using spray pyrolysis deposited nano-crystalline CdO thin films. Journal of Surfaces and Interfaces 17 (2019) 100339.

[32]. N. Singh, P. Singh, M. Singh, D. Gangopadhyay, S. Singh, P. Tandon. Development of a potential LPG sensor based on a PANI–Co3O4 nanocomposite that functions at room temperature. New Journal of Chemistry 43 (2019) 17340.

[33]. G. Singh, R. C. Singh. Highly sensitive and selective liquefed petroleum gas sensor based on novel ZnO–NiO heterostructures. Journal of Materials Science: Materials in Electronics 30 (2019) 20010-20018.

[34]. R. Sonkera, B. Yadav, V. Gupta, M. Tomar. Fabrication and characterization of ZnO-TiO2-PANI (ZTP) micro/nanoballs for the detection of flammable and toxic gases. Journal of Hazardous Materials 370 (2019) 126-137.

[35]. B. Thomas, S. Deepa, K. Kumar. Influence of surface defects and preferential orientation in nanostructured Ce-doped SnO2 thin films by nebulizer spray deposition for lowering the LPG sensing temperature to 150 °C. Journal of Ionics 25 (2019) 809–826.

[36]. H. Dehkordi, A. Mokhtari, K. Dastafkan, V. Soleimanian. Sol–Gel Spin-Coating Followed by Solvothermal Synthesis of Nanorods-Based ZnO Thin Films: Microstructural, Optical, and Gas Sensing Properties. Journal of Electronic Materials 48 (2019) 2.

[37]. M. Taheri, Z. Feizabadi, S. Jafari, N. Mansour. Fast Response and High Sensitivity of Reduced Graphene Oxide/Gold Nano-hybrid for LPG Sensors at Room Temperature. Journal of Electronic Materials 47 (2018) 12.

[38]. K. Khojiera, F. Teimoorib, S. Zolghadrb, M. Pashazanousi. Fast and low concentration detection of liquefied petroleum gas by Auactivated ZnO sensor. Journal of Materials Research Bulletin 108 (2018) 96-100.

[39]. A. Lokhande, A. Yadav, J. Lee, M. He, S. Patil, V. Lokhande, C. Lokhande, J. Kim. Room temperature liquefied petroleum gas sensing using Cu2SnS3/CdS heterojunction. Journal of Alloys and Compound 709 (2017) 92-103.

[40]. A. Singh, A. Singh, S. Singh, P. Tandona. Fabrication of copper ferrite porous hierarchical nanostructures for an efficient liquefied petroleum gas sensor. Journal of Sensors and Actuators B 244 (2017) 806-814.

[41]. S. Kotresh, Y. Ravikiran, S. Tiwari, S. Kumari. Polyaniline–Cadmium Ferrite Nanostructured Composite for Room-Temperature Liquefied Petroleum Gas Sensing. Journal of Electronic Materials 46 (2017) 8.

[42]. S. Kotresh, Y. Ravikirana, S. Kumari, C. Ramana, K. Batoo. Solution based–spin cast processed LPG sensor at room temperature. Journal of Sensors and Actuators A 263 (2017) 687-692.

[43]. Nolwazi N. Shozi, Ioannis Kortidis, Prince S. Mkwae, Nelisiwe P. Chonco, Nompumelelo Leshabane, Mudalo Jozela, Robin E. Kroon, Hendrik C. Swart, Steven S. Nkosi. Extremely sensitive and selective flammable liquefied hydrocarbon gas sensing and inter-dependence of fluctuating operating temperature and resistance: Perspective of rare-earth doped cobalt nanoferrites. Journal of Alloys and Compounds 859 (2021) 157846.

[44]. A. Kumar, J. Shen, W. Yang, H. Zhao, P. Sharma, D. Varshney, Q. Li. Impact of Rare Earth Gd3+ Ions on Structural and Magnetic Properties of Ni0.5Zn0.5Fe2−xGdxO4 Spinel Ferrite: Useful for Advanced Spintronic Technologies. Journal of Superconductivity and Novel Magnetism (2018) 31:1173–1182.

[45]. T. Zhou, S. Cao, R. Zhang, J. Tu, T. Fei, T. Zhang. Effect of cation substitution on the gas sensing performances of ternary spinel MCo2O4 (M= Mn, Ni, and Zn). Journal of applied Materials Interfaces. 11 (2019) 28023-28032.

CHAPTER 3

3. EXPERIMENTAL TECHNIQUES AND SYNTHESIS PROCEDURE

The following stages are involved in the fabrication and testing of semiconducting metal-oxide-based gas sensors: synthesis, characterisation, fabrication, and gas testing.

3.1. Synthesis

In section 2.1.1, various methods of preparing nanomaterials have been concisely described. In more detail, hydrothermal synthesis is categorised as a liquid phase chemical method **[1]**. It is carried out under high temperature and high-pressure conditions. Usually, the starting materials are dissolved in a beaker of distilled/deionised water and mixed properly with a magnetic stirrer at a constant speed. The formation of the desired compound begins when a precipitant is added to the properly mixed solution. The pH is a critical factor in the formation of the desired compound **[2]** and control of crystallite size **[3]**. Thereafter, the precipitate is transferred into an autoclave, which is then sealed and placed in the lab oven, set to a particular temperature, for the reaction to take place and crystal growth to occur **[1,3]**. The autoclave is allowed to cool down slowly to room temperature once the reaction time has elapsed. This method is referred to as solvothermal if other solvent than distilled/deionised water or glycols is used to dissolve the precursor. The hydrothermal method is suitable for the synthesis of various powder nanomaterials. It is environmentally friendly.

In this work, glycolthermal- a method closely related to hydrothermal synthesis- was used to prepare the samples. The only difference was the use of ethylene-glycol as the reaction solvent instead of distilled water and reaction took place in a pressure reactor instead of a lab oven. The glycolthermal method allows the control of ambient

conditions during the reaction; this which makes it effective in the preparation of the spinel **[4]**.

3.2. Characterisation techniques of powdery nanomaterials

3.2.1. Introduction

The study of properties of materials is a significant consideration in nanoscience and nanotechnology. Earlier in time, the investigation of properties of materials was done by visual inspection. However, the advances in science and technology have led to the development of better and more reliable techniques to study the properties of materials **[5]**. Nanomaterials are described as materials with at least one dimension of the order of 1-100 nm **[6]**. They exhibit mechanical, electrochemical, thermal, optical, magnetic, electrical, chemical, and structural properties owing to their high volume-to-surface ratio, small grain size, triple junction significant volume fraction of grain boundaries, and a significant fraction of surface atoms **[6]**. To ascertain these properties, techniques such as Ultraviolet Visible Spectroscopy (UV-Vis), photoluminescence (PL) spectroscopy, X-Ray Diffractometry (XRD), X-ray Photoelectron Spectroscopy (XPS), Brunauer-Emmett-Teller (BET) surface area analysis, Thermogravimetric Analysis (TGA), Scanning Electron Microscopy (SEM), and High Resolution Transmission Scanning Electron Microscopy (HRTEM) have been developed. Table 3.1 shows some characterization techniques and basic information obtained from them. The remaining part of this section will discuss only the characterisation techniques that were used in this study.

3.2.2. X-ray diffractometry

Since X-ray was discovered in 1895 by the German physicist- Röntgen, it has been used to study the internal organs of human body and the internal structure of opaque objects owing to their high penetrating power **[7]**. Later, it was used to study the

structure of matter. X-rays are electromagnetic radiation possessing the same characteristics as visible light but of shorter wavelength and higher penetrating power. Its characteristic high penetrating power makes it applicable in radiography and diffractometry. The wavelength of X-rays used in diffraction is within the range 0.5-2.5 Å **[8]**.

Table 3.1. Characterisation techniques of powdery nanomaterials and their significance **[9, 10]**

Characterisation techniques	**Main information obtained**
XRD	Composition, crystal structure, crystallite/grain size
XPS	Elemental composition, oxidation states, electronic structure
UV-Vis	Optical properties, agglomeration state, concentration, size
PL spectroscopy	Electronic structure, optical properties related to structural features such as size, composition, defects
TGA	Thermal stability from inspection of change in mass
BET	Surface area
SEM	Morphology, dispersion of nanoparticles, precision in lateral dimensions of nanoparticles, elemental composition.
HRTEM	Morphology and the surface structure at an atomic level, defect study

Figure 3.1 shows a schematic of an X-ray diffractometer for characterisation of powder samples. Characterisation by X-ray diffractometer is based on the measurement of X-ray intensities and scattering angle of the diffracted ray leaving the powder specimen.

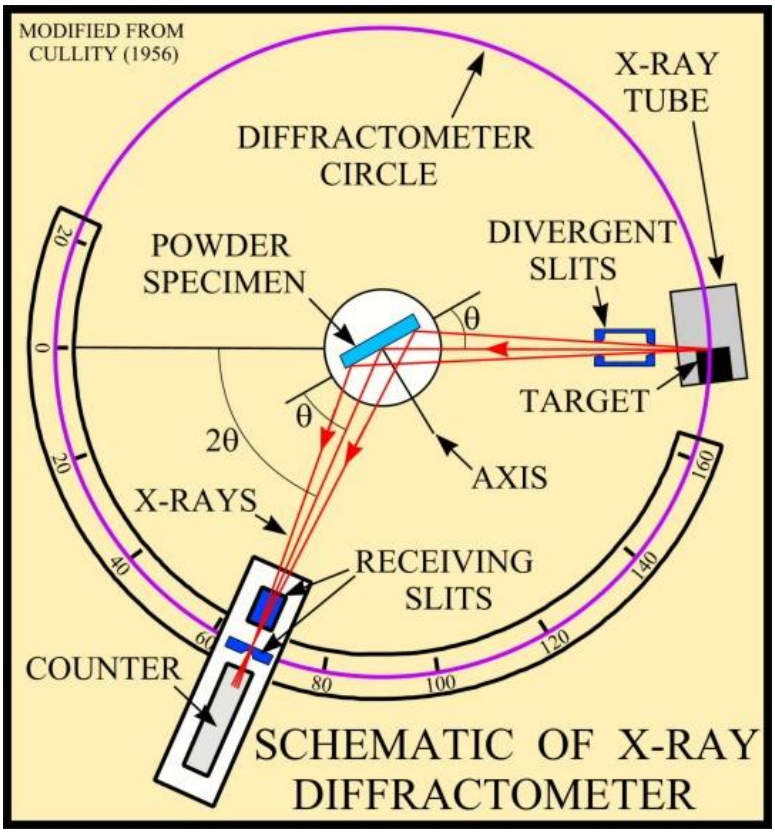

Figure 3.1. Schematic of an x-ray diffractometer with powder sample (Adapted from U. S. Geological Survey Open-File Report 01-041).

In X-ray diffractometry, X-rays are generated in an X-ray tube and focused on the samples at an incident angle; the diffracted rays are then collected, processed, and counted to determine the crystal structure of the samples. From X-ray diffraction analysis other obtainable information includes crystallite size, growth orientation, and symmetry of unit cell.

3.2.3. X-ray photoelectron spectroscopy

This technique is used for investigation of surface composition of a sample by revealing the elements that are present at the surface and the chemical bond that

exists between them. It can detect all elements except helium and hydrogen. This technique is based on the photoemission effect. When the X-ray bombards a sample, some electrons receive enough excitation energy to leave the atom. These escaped electrons are collected by an electron analyser which then quantifies their kinetic energy. The electron analyser is designed to produce energy spectrum of intensity against binding energy. Each energy peak on the spectrum corresponds to a specific element while each peak area, i.e., intensity of the peak, is proportional to the number of atoms present in each element. The analyser, therefore, reveals the elements in the sample and gives the amount of element **[11]**.

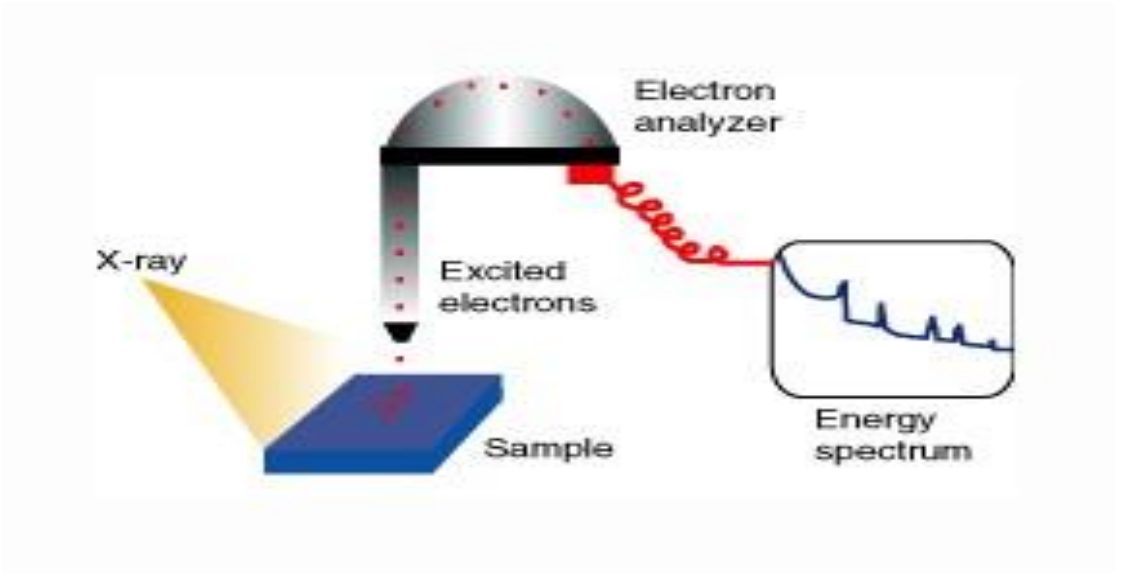

Figure 3.2. Schematic diagram of an X-ray photoelectron spectroscope (Adapted from the actinide research quarterly: 2nd quarter 2004. www.lanl.gov).

3.2.4. Scanning electron microscopy

In this technique, a focused beam of high-energy electrons is used to generate a variety of signals on the sample surface **[12]**. The signal resulting from electron-sample interaction is used to obtain information about morphology, dispersion of nanoparticles, precision in lateral dimensions of nanoparticles, and elemental composition.

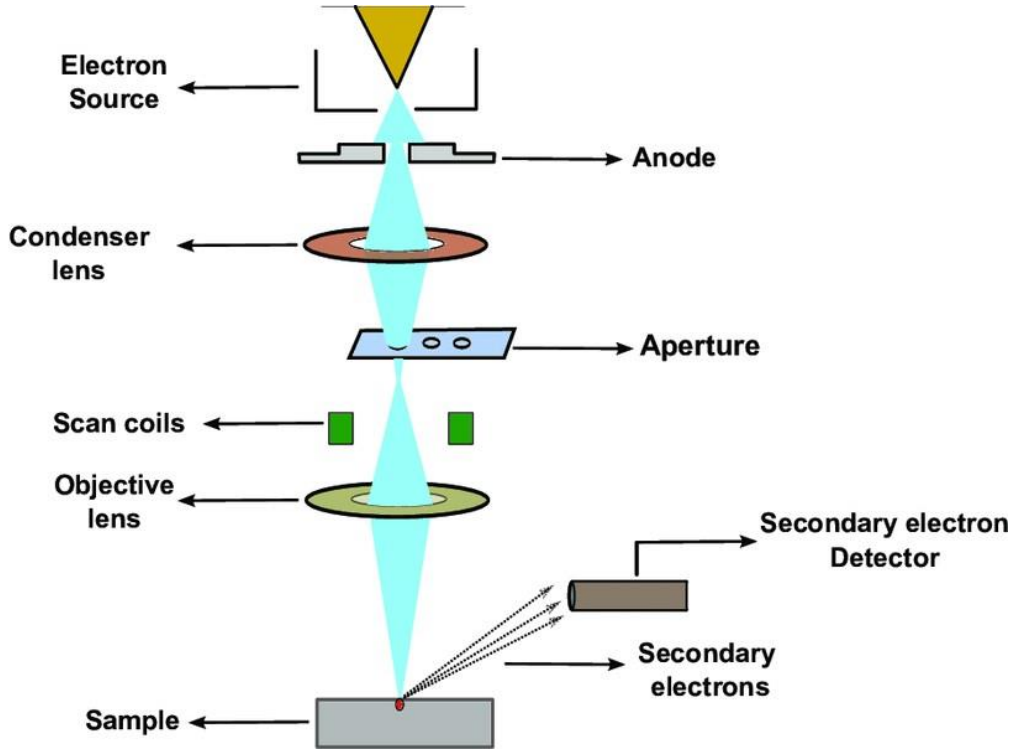

Figure 3.3. Schematic diagram of a scanning electron spectroscope (Adapted from https://www.researchgate.net/publication/281534044_vision_and_visual_servoing_for_nanomanipulation_and_nanocharacterization_in_scanning_electron_microscope 15/01/2022).

3.2.5. High resolution transmission electron microscopy

In this technique, an electron beam is directed onto a sample. When the beam strikes the sample (labelled 'specimen' in figure 3.4), it scatters in the opposite direction. Both transmitted and scattered beams are combined to form a high-resolution image of the atomic structure of the sample, which can be viewed on the cathode ray tube system. Constructive and destructive interference of electrons diffracted as they pass through the sample resulting in the formation of image contrast **[13]**. Through this process, the defect, morphology, and surface structure at an atomic level are studied

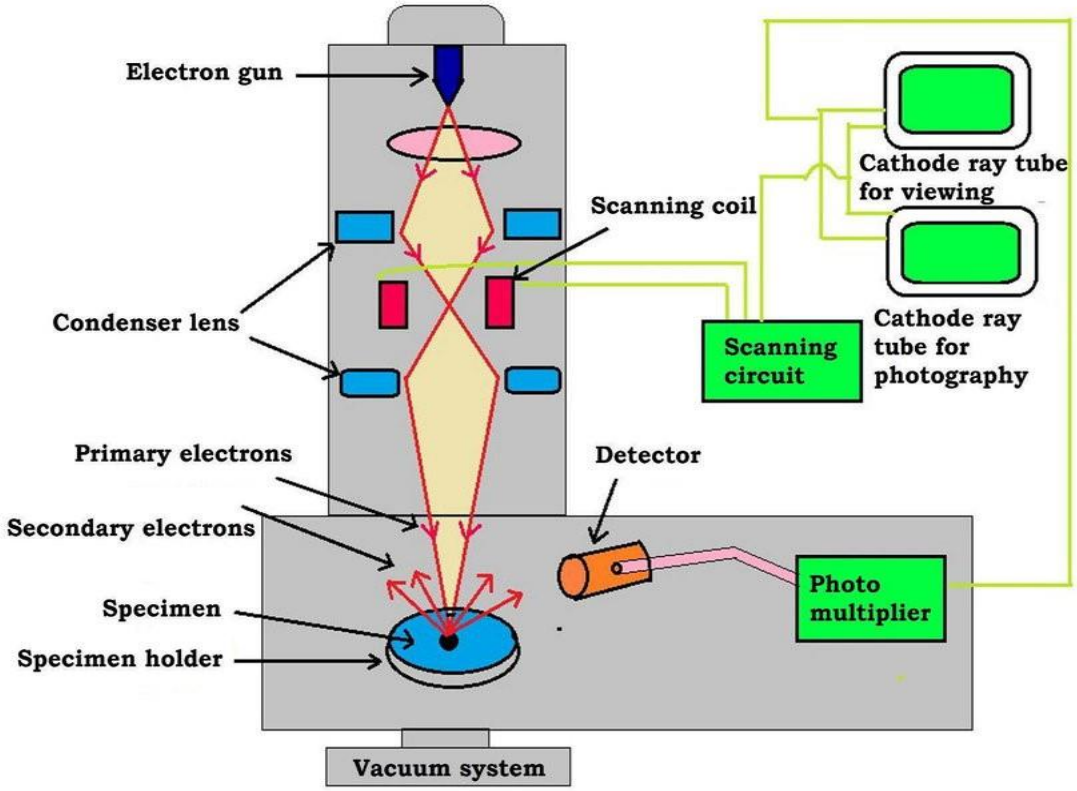

Figure 3.4. Schematic diagram of a high-resolution transmission electron microscope (Adapted from https://www.researchgate.net/publication/341277064_synthesis_of_silver_nanoparticles_using_silk_fibroin_characterization_and_potential_antibacterial_properties 2022).

3.2.6. Brunauer-Emmett-Teller surface area analysis

This is a technique used for determining the mass-specific or volume-specific surface area of a powder sample. Figure 3. 1 shows the schematic of surface area analyser for BET characterisation. In BET surface area analysis, nitrogen gas is gradually released into the sample cell until saturation pressure is reached i.e. there can be no further adsorption **[14]**. Once the adsorption layers are formed, the sample is removed, heated to release the adsorbed nitrogen from the material, and then quantified. From the data collected, a graph of the amount of gas adsorbed as a function of the relative pressure is plotted.

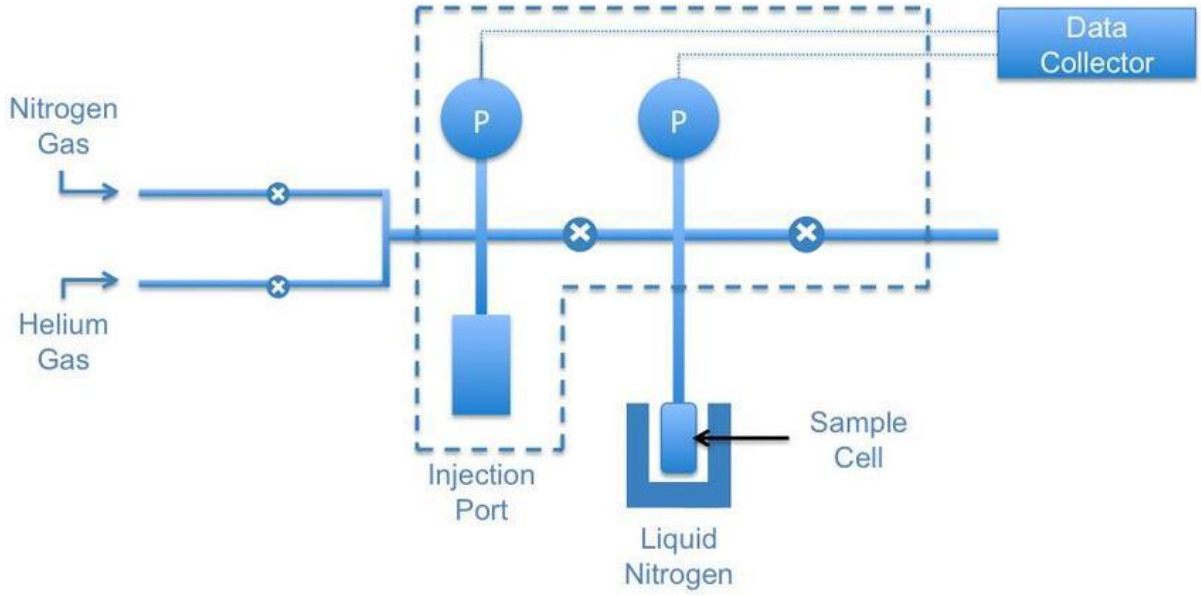

Figure 3.5. The schematic of surface area analyser for BET characterisation (Adapted from https://www.researchgate.net/publication/316673131_development_of_electrodes_for_artificial_photosynthetic_system 2022).

3.3. Method of sensor fabrication

There are different methods of fabricating gas sensors, one of which is drop-casting: the method employed in this work. Materials and apparatuses required for this technique are *test vial, ultrasonic cleaner (sonicator), pipette,* and *substrate.* Figures 3.6(a and b) show a sonicator and a fabricated sensor.

i. Test vial: this apparatus is needed for mixing the powder sample with ethanol to form a suspension.

ii. Ultrasonic cleaner: this is also known as the sonicator. It uses sound waves to agitate particles, thereby ensuring proper mixing and accelerated dissolution of the sample in ethanol.

iii. Pipette: this is used for mixing and sucking the dissolved sample from the test vial and depositing onto a substrate where a thin film is formed.

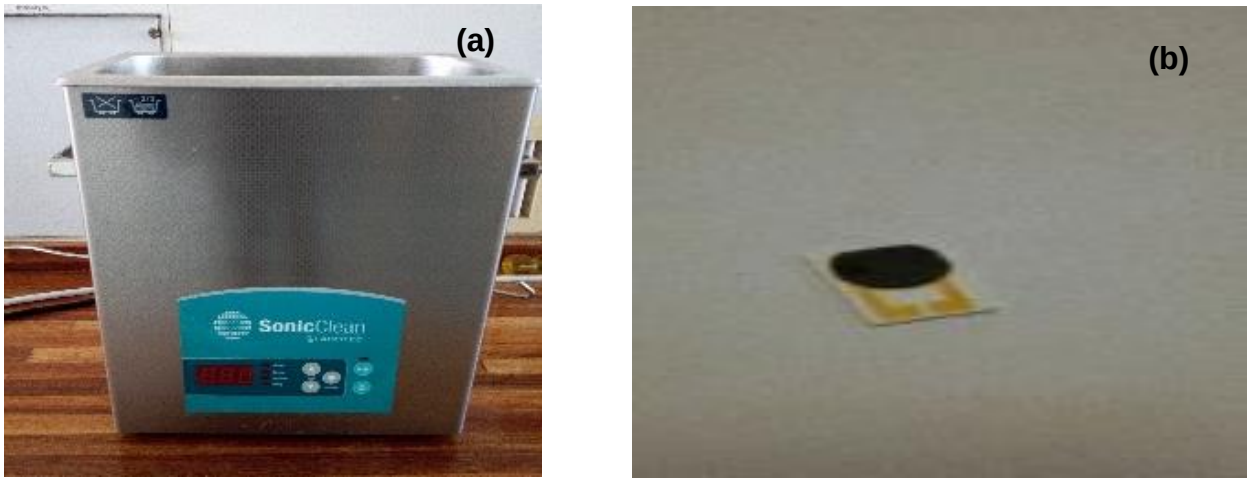

Figure 3.6. (a) a sonicator, (b) a fabricated sensor.

iv. Substrate: the substrate is usually made of alumina screen-printed with gold or platinum electrode. Figure 3.6(b) shows a substrate screen-printed with gold electrode. The thin dark layer on top of the substrate is the sensing surface made by dropping the mixture.

3.4. Gas testing technique

At this stage, the sensors are exposed to various gases to ascertain their gas sensing performance. Figures 3.7(a-d) show the gas testing system (and some of its features) available in the Physics department of the University of Zululand.

i. The climatic gas testing chamber is an enclosure where chemical reaction takes place between the analyte gas and the sensor. It is situated inside the gas testing system.

ii. The gas lines convey the gas from the cylinder in an outside storage room into the chamber.

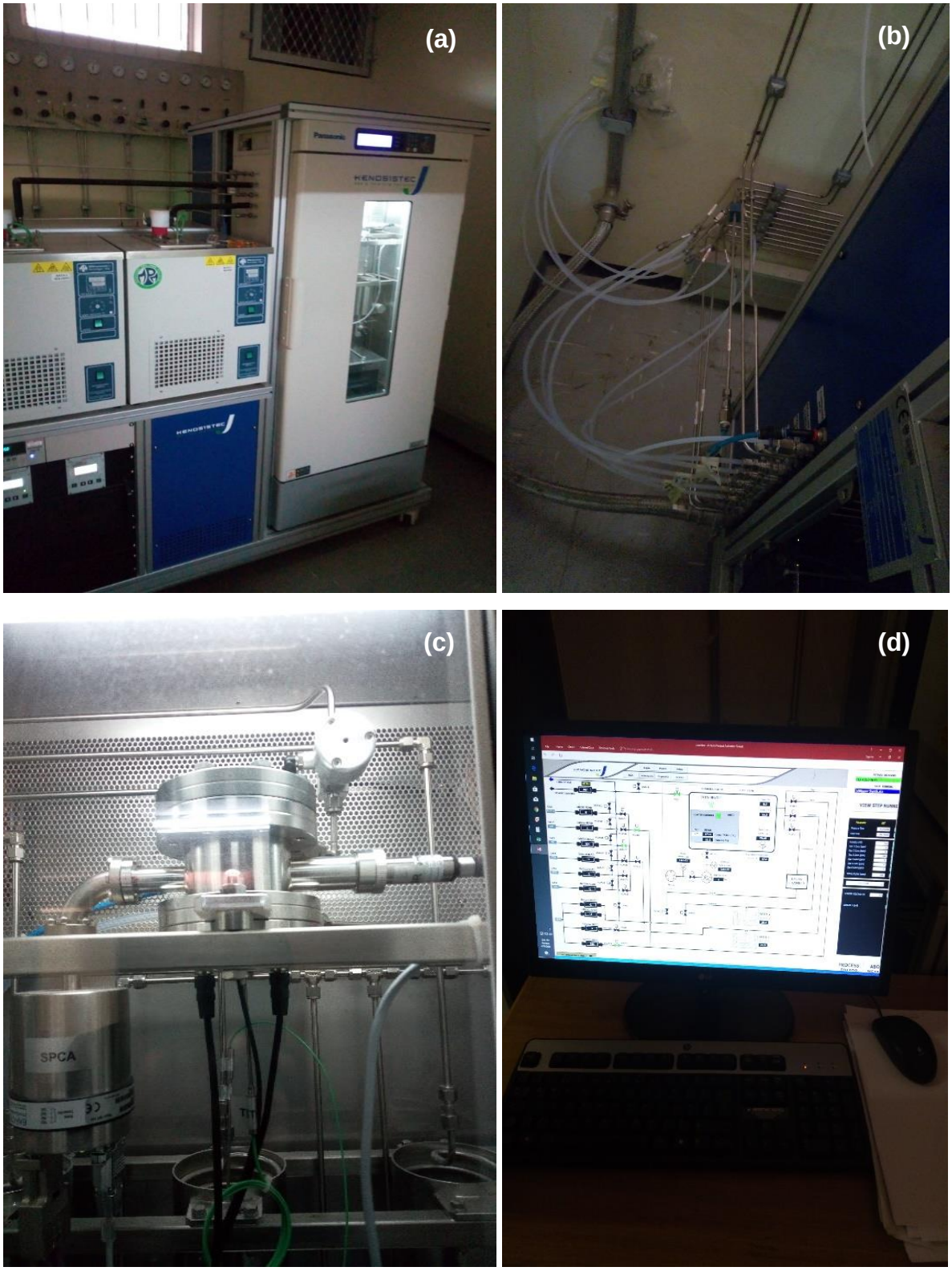

Figure 3.7. (a) KSGAS6S gas testing system, (b) gas lines, (c) the climatic gas testing chamber, (d) computer system.

iii. The computer system is adapted to the gas testing system for programming and to record the change in the electrical resistance or current resulting from the interaction taking place within the chamber.

The gas testing system has some other important features, such as valves and a humidity bath. The valves regulate gas flow into the chamber and the humidity bath is for creating a humid atmosphere in the testing chamber when it is necessary to carry out humidity test on a sensor.

References

[1]. Y. Li, Y. Lu, K. Wu, D. Zhang, M. Debliquy, C. Zhang. Microwave-assisted hydrothermal synthesis of copper oxide-based gas-sensitive nanostructures. Journal of Rare Metals 40 (2021)1477–1493.

[2]. M. Kasim, N. Kamarulzaman, R. Rusdil, A. Rahman. Effect of pH on the crystal growth of ZnO nanomaterials and their band gap energies. Journal of Physics: Conference series 1083 (2018) 102043.

[3]. G. Yang, S. Park. Conventional and Microwave Hydrothermal Synthesis and Application of Functional Materials: A Review. Journal of Materials 12 (2019) 1177.

[4]. T. Nhlapo, T. Mokoena, J. Msomi, T. Moyo, T. Mahule, M. Nyathi. Synthesis, Electron Spin Resonance and Photoluminescence properties of Sm3+ ion doped Zn-Mn nanoferrites synthesized by glycol-thermal method. Journal of Molecular Structure 1268 (2022) 133703.

[5]. D. Bryce. NMR crystallography: structure and properties of materials from soli-state nuclear magnetic resonance observables. International Union of Crystallography Journal 4 (2017) 350-359.

[6]. L. Kolahalam, I. Viswanath, B. Diwakar, B. Govindh, V. Reddy, Y. Murthy. Review on nanomaterials: synthesis and applications. Materialstoday: Proceedings 18 (2019) 2182-2190.

[7]. N. parab, J. Barnes, C. Zhao, R. Cunningham, K. Fezzaa, A. Rollett, T. Sun. real time observation of binder jetting printing process using high-speed x-ray imaging. Nature 9 (2019) 2499.

[8]. H. Cheng, C. Lu, J. Liu, Y. Yan, X. Han, H. Jin, Y. Wang, Y. Liu, C. Wu. Synchrotron radiation X-ray powder diffraction techniques applied in hydrogen storage

materials- A review. Progress in Natural Science: Materials International 27 (2017) 66-73.

[9]. S. Mourdikoudis, R. Pallares, N. Thanh. Characterization techniques for nanoparticles: comparison and complementarity upon studying nanoparticle properties. Journal of Nanoscale 10 (2018) 12871-12934.

[10]. Y. Deng. Common Phase and Structure Misidentifications in High-Resolution TEM Characterization of Perovskite Materials. Journal of Condensed Matter 1 (2021) 6.

[11]. X. Chen, X. Wang, D. Fang. A review on C1s XPS-spectra for some kinds of carbon materials. Journal of Fullerenes, Nanotubes and Carbon Nanostructures 28 (2020) 1048–1058.

[12]. N. Ural. The significance of scanning electron microscopy(SEM)analysis on the microstructure of improved clay: An overview. Journal of Open Geosciences 13 (2021) 197–218.

[13]. P. Toth. Nanostructure quantification of turbostratic carbon by HRTEM image analysis: State of the art, biases, sensitivity and best practices. Carbon, Elsevier 178 (2021) 688-707.

[14]. M. Naderi. surface area: Progress in filtration and separation, Elsevier (2015) 585-608.

CHAPTER 4

4. EXPERIMENTAL DETAILS, RESULTS AND DISCUSSION

4.1. Introduction

This chapter presents the *experimental details* of this work, the *results* and the *discussion*. Section 4.2 (experimental details) discusses the synthesis of the powder samples, the characterisation techniques applied (X-Ray Diffraction analysis (XRD), X-ray Photoelectron Spectroscopy (XPS), Scanning Electron Microscopy (SEM), High Resolution Scanning Electron Microscopy (HRTEM), Brunauer-Emmett-Teller surface area analysis (BET)), and the gas sensing measurement. Section 4.3 includes the result and the discussion.

4.2. Experimental details

4.2.1. Glycolthermal synthesis of $Co_{1-2x}Ni_xMn_xCe_yFe_{2-y}O_4$ powders

$Co_{1-2x}Ni_xMn_xFe_{2-y}Ce_yO_4$, where x = y = 0.0, 0.1, 0.2 and 0.3, were prepared via the glycolthermal technique. Stoichiometric amounts of the precursors: $CoCl_2.6H_2O$ (97 %), $NiCl_2.6H_2O$ (98 %), $MnCl_2.4H_2O$ (99 %), $CeCl_3.7H_2O$ (99.9 %), and $FeCl_3.6H_2O$ (98 %) were dissolved in 100 mL of distilled water. The pH of the solution was adjusted to 10 by adding Ammonium hydroxide solution dropwise and was mixed by vigorous stirring using a magnetic stirrer for 1h. The precipitate was then washed several times using deionised water and tested for the presence of chlorides using silver nitrates standard solution. The cleaned precipitate (free of chloride ions) was added to 300 mL of ethylene glycol. The precipitate was allowed to react on a PARR 4843 Watlow series stirred pressure reactor for 6 hours at 200 °C with reaction pressures ranging from 50 to 100 psi at a stirring speed of 300 rpm. The glycol-reacted precipitate was washed using deionised water and the precipitate was heated rapidly to 200 °C for 4 hours in the open air and cooled down to room temperature to obtain the as-prepared samples;

while some portion of the sample for which x = y = 0 (i.e. $CoFe_2O_4$) was left to dry overnight under a 250 W infrared lamp. The samples were then annealed at 500 °C for 3 hours to obtain the final products.

4.2.2. Characterisation of the powder samples

The crystal structure of these powder samples was characterised by using a Bruker D8 Advance X-ray diffractometer fitted with Cu-Kα (λ = 0.1541 nm) radiation source with a scan rate of 0.3° per minute. Images of the surface morphology and particle size of the powder samples were captured using a scanning electron microscope (SEM, Carl ZEISS Sigma VP-03-67). High-resolution transmission electron microscopy (HR-TEM) images were recorded using a JEOL 1400 system. A PHI 5000 Scanning ESCA Microprobe was used to examine the chemical state of the samples by X-ray photoelectron spectroscopy (XPS) analysis using an A 100 μm diameter monochromatic Al Kα (1486.6 eV) X-ray beam at a pressure of 9.3×10^{-10} Torr. The samples were sputter-etched using Ar^+ with an energy of 2 kV and 2 μA for 1 minute. The sputter rate was 15 nm per minute. A low energy Ar^+ ion gun and low energy neutraliser electron gun were used to minimise charging on the surface. The binding energy calibration was done using the high energy peak of Cu 2p3 at 932.62 eV and the low energy peak of Au 4f7 at 83.96 eV. The retard linearity was set in order to keep the difference between these two peaks constant at 848.66 eV. The work function of the analyser was set to 3.7 eV for the Ag3d5 peak to be at 368.27 ± 0.1 eV. N_2 adsorption-desorption isotherms and Brunauer-Emmett-Teller (BET) surface area studies were performed using a Micromeritics TRISTAR II (USA) surface area analyser. The samples were degassed at 150 °C for 3 hours. The BET surface area, pore size, and pore volume were measured using nitrogen at 77 K.

4.2.3. Fabrication of sensors and gas sensing measurements

To fabricate the gas sensors, each powder sample was evenly distributed in ethanol and sonicated for 2 h. Then the resulting solution was drop-casted onto an alumina substrate pre-printed with gold electrode on the top surface. The bottom surface of the substrate was heated to 90 °C for the organic solvent to vaporise and leave a dry well adhering sensing layer. Thereafter, the sensors were simultaneously placed in an airtight chamber with electrical and gas feeds for sensing measurement. The measurements of the target gases (LPG, NH_3, ethanol, and propanol) at different ppm concentrations, were conducted using a KS026K16 (KENOSISTEC model, Italy) gas testing system. These measurements were performed at different operating temperatures of 175 and 225 °C under a constant applied voltage of 5.0 V across the sensor. Dry air (79% N_2 and 21% O_2) was used to carry the gases into the chamber for measurements. For gas sensing measurement in a reduced oxygen environment, inert gases: helium, argon, and nitrogen were used as carrier gas. The gas sensing measurements were conducted in dry air ambient (0.1 %RH). The change in the sensor resistance of the device was quantified using a Keithley 6487/E picoammeter/voltage source meter. The sensor response, S, was calculated using equation 4.1

$$S = \frac{\mathrm{I}_g}{I_a} \qquad (4.1)$$

where I_g is the current in the presence of gaseous species and I_a is the current in the air.

4.3. Results and discussion

4.3.1. X-ray diffraction, surface morphology and chemical composition

Figure 4.1 depicts the X-ray diffraction patterns of the undoped $CoFe_2O_4$ that was dried using an infrared (IR) lamp and oven at 200 °C (natural dried).

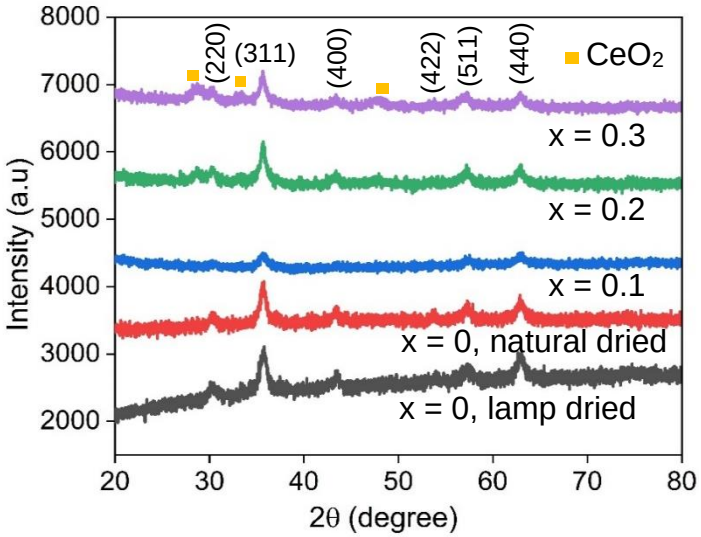

Figure 4.1. The XRD patterns of cobalt ferrite spinel doped with Ni & Mn in tetrahedral site, Ce at octahedral site. SEM images of the Co1-2xNixMnxFe2-yCeyO4 samples with (a) x = y = 0: dried with infrared lamp, (b) x = y = 0: dried naturally, (c) x = y = 0.1, (d) x = y = 0.2 and (e) x = y = 0.3.

The figure further shows double a substitution of Ni, Mn and Ce in the tetrahedral A-site and octahedral B-site of the $Co_{1-2x}Ni_xMn_xFe_{2-y}Ce_yO_4$, respectively. These substitutions were made at equal content with both x and y chosen between $0 \leq x = y \leq 0.3$. These substituted spinel nanoferrites were natural-dried and were all subjected to annealing as described in the experimental section earlier.

The final products following the appropriate substitutions were $Co_{0.8}Ni_{0.1}Mn_{0.1}Fe_{1.9}Ce_{0.1}O_4$, $Co_{0.6}Ni_{0.2}Mn_{0.2}Fe_{1.8}Ce_{0.2}O_4$, and $Co_{0.4}Ni_{0.3}Mn_{0.3}Fe_{1.7}Ce_{0.3}O_4$ spinel ferrites. The diffraction patterns of the samples having peaks at 2θ positions are indexed as follows: 30.18° (220), 35.58° (311), 43.39° (400), 53.82° (422), 57.23° (511), and 62.91° (440). This is in good agreement with the literature **[1-5]** and confirmed the formation of the cubic spinel structure with a PDF card no. 96-154-0974. The additional peaks observed at 2θ positions 28.63, 33.10 and 47.87° correspond respectively to (111), (200) and (220) planes of CeO_2 peaks with PDF card no. 96-721-7888 **[4, 6-8]**, indicating the formation of CeO_2 secondary phase in the spinel structure which started to occur at y = 0.2 and became more prominent

at y = 0.3. No other impurities corresponding to Ni and Mn oxides were observed. The ionic radii of Ni^{2+}, Mn^{2+}, and Co^{2+} are very close to each other with 0.083, 0.081, and 0.079 nm, respectively. However, the ionic radius of Ce^{3+} (0.101 nm) is greater than that of Fe^{3+} (0.064 nm). As a result, the formation of the cerium dioxides as a secondary phase is due to the difference in the ionic radii. Mkwae et al. **[9]** have observed the formation of the CeO_2 as a secondary phase at higher Ce doping content during the synthesis of $MgFe_{2-x}Ce_xO_4$ by the hydrothermal chemical process. Likewise, many other researchers observed this secondary phase of CeO_2 when Ce^{3+} was substituted in their spinel nanoferrites **[4, 10-12]**. The crystallinity of the sample with x = y = 0.1 is less than that of the other samples as some peaks corresponding to the spinel appear to be absent or inconspicuous because of their low intensity. The crystallite sizes of the samples were calculated using the Debye-Scherrer equation and are presented in table 4.1.

Table 4.1. The crystallite sizes, pore size distribution and the BET specific surface areas of the samples.

$Co_{1-2x}Ni_xMn_xFe_{2-y}Ce_yO_4$	D_{311} (nm)	Pore Size (nm)	Spec. surf. Area (m^2/g)
x = y = 0, lamp-dried	9.99	11.38	66.99
x = y = 0, natural-dried	11.30	11.96	62.48
x = y = 0.1	9.28	12.34	72.82
x = y = 0.2	12.05	10.52	51.93
x = y = 0.3	12.30	13.29	60.76

Figures 4.2(a-e) shows the scanning electron microscope (SEM) images of the un-substituted and double substituted spinel nanoferrites samples. Both the $CoFe_2O_4$, natural dried and IR lamb dried spinels in figures 4.2(a-b), possess similar surface morphology- there are predominantly fine particles with few agglomerates. On addition of substitution to the spinel structure, difference in surface morphology becomes distinct especially on the x = y = 0.1 shown in figure 4.2(c). This sample contains more

agglomerates than fine nanoparticles as compared to the previous two samples with no impurities - Ni, Mn, and Ce atoms. The formation of these closely packed agglomerates could be due to the introduction of the Ni, Mn, and Ce dopants into the spinel, which may complicate the structure. In this substitution, x = y = 0.1, the formation of spinel crystallinity was decreased as observed earlier in the x-ray diffraction (XRD) analysis. At x = y = 0.2, the spinel looks like solidified magma, covered by sparse agglomerates (see figure 4.2d). The spinel crystallinity was increased giving the high XRD peak intensities in Figure 4.1 with secondary phases corresponding to the CeO_2. The sample depicted in Figure 4.2(e) has the appearance of tightly bound particles.

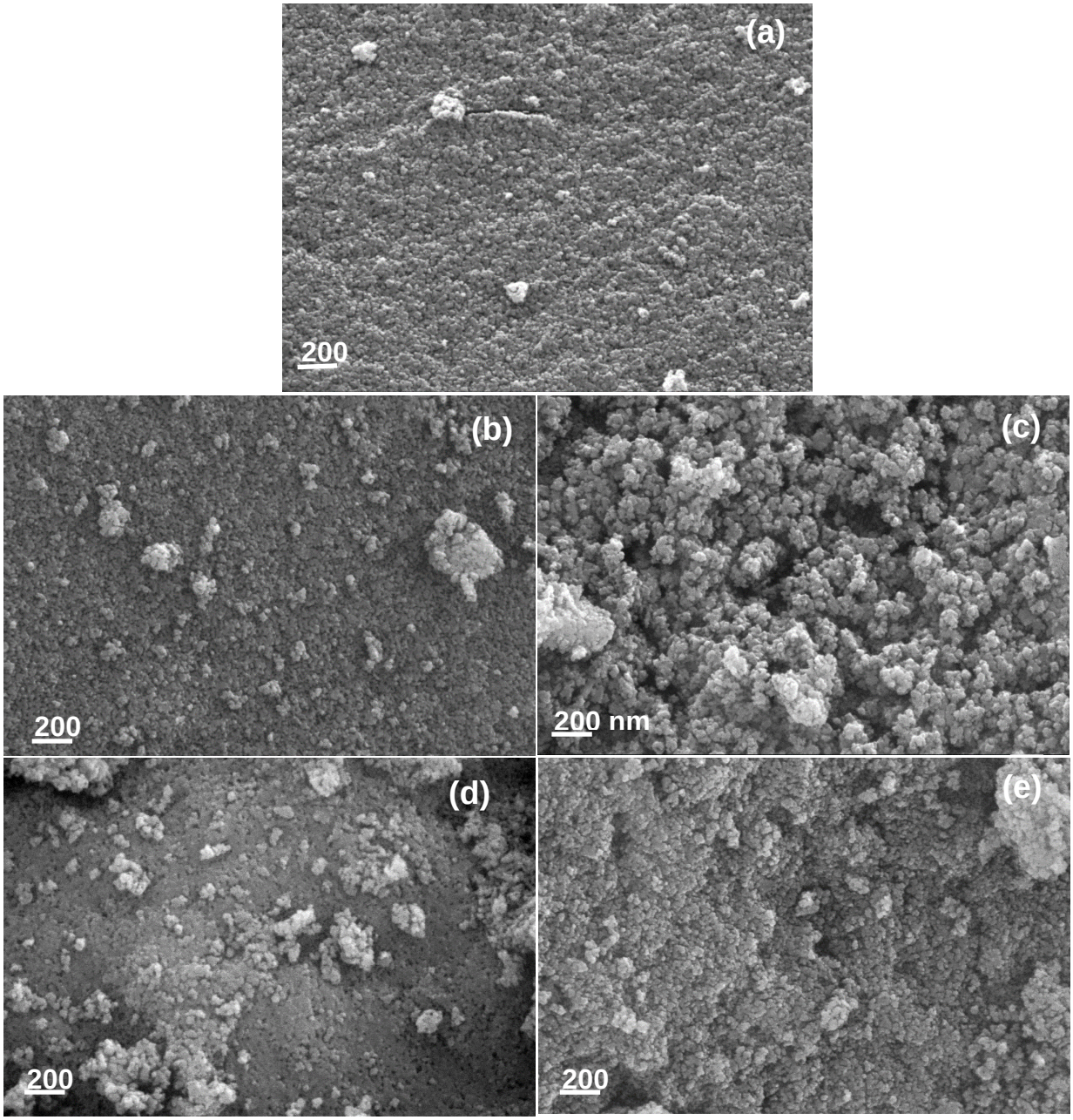

Figure 4.2. SEM images of the Co1-2xNixMnxFe2-yCeyO4 samples with (a) x = y = 0: dried with infrared lamp, (b) x = y = 0: dried naturally, (c) x = y = 0.1, (d) x = y = 0.2 and (e) x = y = 0.3.

The High-Resolution Transmission Electron Microscope (HRTEM) images of the spinel nanoferrites are presented in figures 4.3(a-e). These spinels show crystalline nanoparticles across all areas. This is evident by the clear fringes seen on the HRTEM micrographs. The inter-planar *d*-spacing (d_{hkl}) fringes of the crystalline plane can be attributed to the most prominent ring indexed (311) in the corresponding selected area electron diffraction (SAED) pattern (in figures 4.3a) and were calculated to be d_{311} =

0.255 nm. This value varies slightly between samples due to changes in lattice parameters as a result of sites loading (especially B-site). It was highly expected that the cubic spinel structure might undergo both expansion and shrinkage between $0 \leq y \leq 0.3$.

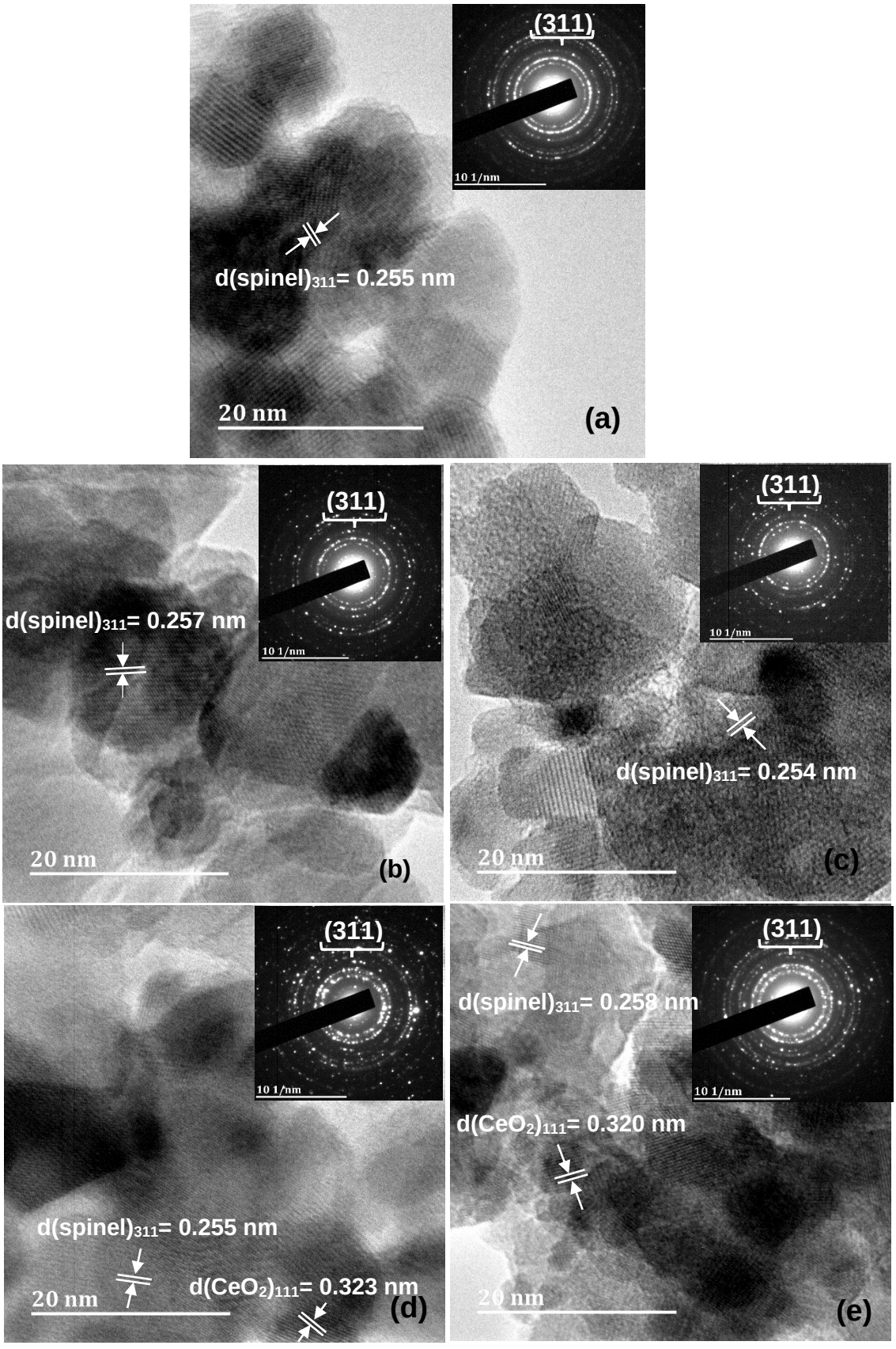

Figure 4.3. HRTEM images of the Co1-2xNixMnxFe2-yCeyO4 samples with (a) x = y = 0: dried with infrared lamp, (b) x = y = 0: dried naturally, (c) x = y = 0.1, (d) x = y = 0.2 and (e) x = y = 0.3. The insets are the corresponding Selected Area Electron Diffraction patterns.

The SAED observed for these nanoferrites show crystalline spotted rings with the (311) reflection as more prominent. The SAED ring corresponding to the CeO_2 can also be observed very close to the most prominent ring of 311 peak. This is consistent with the XRD result and the ring corresponds to the (111) plane of CeO_2 fluorite structure **[13]** whose inter-planar distance (*d*-spacing) is 0.32 nm. It is worthy of mention that, the secondary phase of CeO_2 can only be formed as Ce^{3+} content is increased in the spinel structure.

Pore sizes and their distribution were estimated by conducting nitrogen adsorption-desorption measurement on the samples. A substance can be microporous (pore size smaller than 2 nm), mesoporous (pore size between 2 and 50 nm) or microporous (pore size greater than 50 nm) depending on its pore size. It is deducible from Table 4.1 that the samples possess mesopores. figure 4.4 depicts the nitrogen adsorption-desorption isotherm of the double-substitution spinels. They are type IV isotherms, characteristic of mesoporous materials. The insets are the corresponding pore size distribution.

Table 4.1 presents the samples with their corresponding crystallite size calculated from the most prominent peak (at (311) plane) of the spinel, pore size and specific surface area. The crystallite sizes vary proportionately with the dopant amount, while the pore sizes and specific surface areas follow a haphazard order.

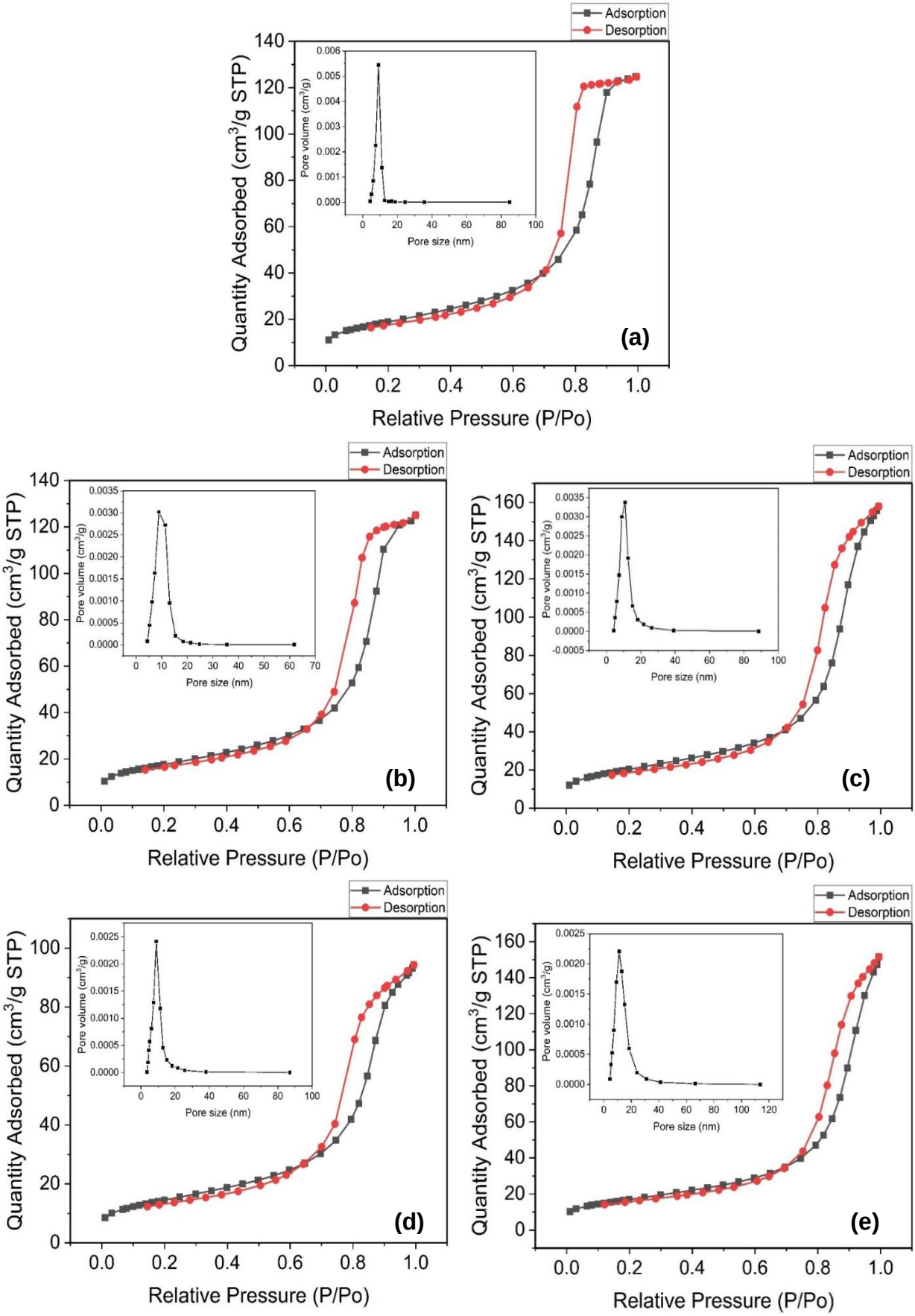

Figure 4.4. Nitrogen adsorption-desorption isotherms of Co1-2xNixMnxFe2-yCeyO4 samples with (a) x = y = 0: dried with infrared lamp, (b) x = y = 0: dried naturally, (c) x = y = 0.1, (d) x = y = 0.2 and (e) x = y = 0.3. Insets: The corresponding pore size distribution.

Figures 4.4-4.8 depict the X-ray photo-electron spectroscopy (XPS) of the $Co_{1-2x}Ni_xMn_xFe_{2-y}Ce_yO_4$ nanoferrites with $0 \leq x = y \leq 0.3$. The survey spectrum of the $CoFe_2O_4$ samples is represented in figure 4.5(a). Figures 4.5(b-d) show the XPS spectra of the lamp-dried $CoFe_2O_4$ sample. The observed peaks confirm the presence of Co, Fe, O, and C elements in the samples. Figure 4.5(b) shows the Co 2p core level spectrum. The fitting peaks at 779.46 eV (due to B-site Co^{2+}) and 781.31 eV (due to A-site Co^{2+}) correspond to Co $2p_{3/2}$ with its satellite at 786.14 eV. Also, the peak due to Co $2p_{1/2}$ is observed at 796.21 eV and its satellite is at 803.53 eV. Fe 2p core level spectrum is revealed in figure 4.5(c). The four fitting peaks corresponding to Fe $2p_{3/2}$ are due to B-site Fe $^{3+}$ (at 709.85 eV) and its satellite (at 714.04 eV) and A-site Fe $^{3+}$ (at 711.53 eV) and its satellite (at 718.49 eV). The peak corresponding to Fe $2p_{1/2}$ and its satellite are observed at 724.56 eV and 732.20 eV respectively. Figure 4.5(d) represents the O 1s core level spectrum. The fitting peak situated at 529.68 eV is attributed to the lattice oxygen. The component at 531. 46 eV is typical of the surface hydroxyl group **[14-16]**, while the third peak centred at 533.24 eV indicates the presence of adsorbed molecular water on the surface **[17]**.

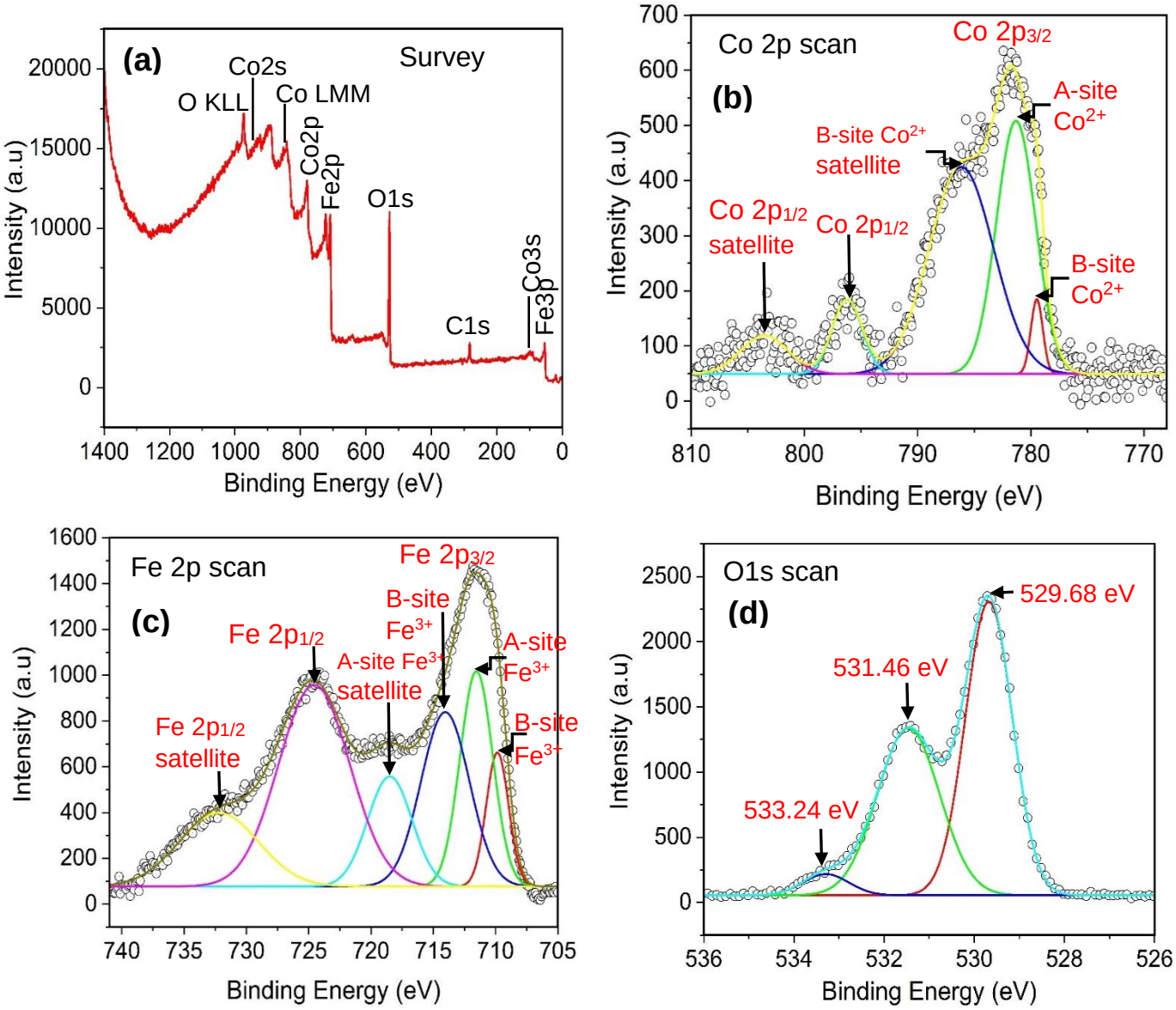

Figure 4.5. (a) Survey spectrum, before sputtering, of CoFe2O4 samples. XPS spectra of Co1-2xNixMnxFe2-yCeyO4 sample for which x = y = 0 (lamp-dried): (b) Co 2p scan, (c) Fe 2p scan, and (d) O 1s scan.

Figure 4.6a portrays the survey spectrum of the doped samples, confirming the presence of Co, Ni, Mn, Fe, Ce, O, and C elements in the $Co_{1-2x}Ni_xMn_xFe_{2-y}Ce_yO_4$ spinel nanoferrites. Figures 4.6(b-d) shows the XPS spectra of the naturally dried $CoFe_2O_4$ sample. The Co 2p core level spectrum (Figure 4.6b) indicates the substitution presence of Co^{2+} in the B-site only. This occurrence is characteristic of the inverse spinel group to which $CoFe_2O_4$ belongs. The peaks centred at 780.39 eV and 785.43 eV are assigned to B-site Co^{2+} (of Co $2p_{3/2}$) and its satellite respectively.

The Co $2p_{1/2}$ peak and its corresponding satellite is located at 795.74 eV and 802.30 eV respectively. Figure 4.6(c), in a very similar manner to the lamp-dried sample, indicates the presence of Fe3+ ions in both B and A sites. The fitting peaks associated with the presence of these ions are located at 710.34 eV (B-site Fe^{3+}) and 712.31 eV (A-site Fe^{3+}) of the Co $2p_{3/2}$ peak. However, the only satellite observed for the Co $2p_{3/2}$ peak (centred at 717.61 eV) can be attributed to A-site Fe^{3+}. The peak due to Fe $2p_{1/2}$ and its corresponding satellite are also observed respectively at 724.49 eV and 730.95 eV. In figure 4.6d, the O 1s core spectrum is portrayed. The peak located at 529.84 is associated with the lattice oxygen (or metal-oxide bond), while the peak situated at 530.93 eV may indicate chemisorbed surface oxygen **[18]**.

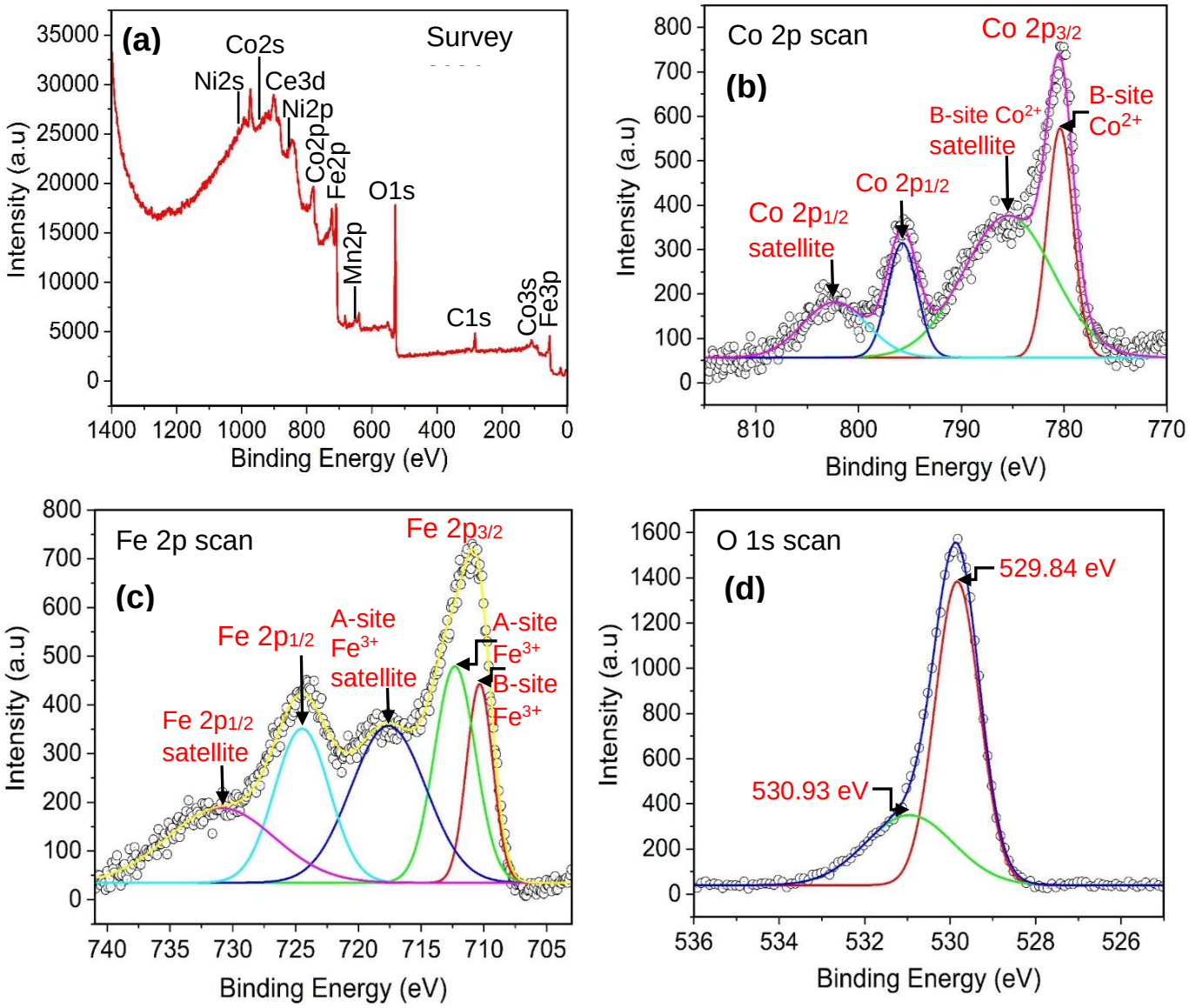

Figure 4.6. (a) Survey spectrum, before sputtering, of Co1-2xNixMnxFe2-yCeyO4 samples. XPS spectra of Co1-2xNixMnxFe2-yCeyO4 sample for which x = y = 0 (natural-dried): (b) Co 2p scan, (c) Fe 2p scan, and (d) O 1s scan.

Figures 4.7(a-f) depicts the X-ray photo-electron spectroscopy (XPS) of the $Co_{1-2x}Ni_xMn_xFe_{2-y}Ce_yO_4$ nanoferrite with x = y= 0.1. Figure 4.6a shows the Co 2p core level spectrum. The fitting peaks at 779.96 eV attributed to B-site Co^{2+} and 781.62 eV which is attributed to A-site Co^{2+}, correspond to Co $2p_{3/2}$ with its satellites at 785.11 eV, while the one at 796.06 eV corresponds to Co $2p_{1/2}$ with its satellite at 803.25 eV. It is conclusive that only Co^{2+} cations are present in the sample, since Co^{3+} cations occupying tetrahedral and octahedral sites normally exhibit peaks centred,

respectively, at 798.5 eV and 783.3 eV **[19]**. Observing from the survey (Figure 4.6(a)), the Ni 2p peak appears to be at the edge of a peak. This may suggest the limited presence or even total absence of Ni in the sample composition. This observation is further confirmed by the Ni 2p scan (Figure 4.7(b)) as the peaks situated at the lower and the higher Binding Energy regions (848.66 eV and 886.12 eV, respectively) of the spectrum could not be ascribed to Nickel. Figure 4.7(c) shows the Mn 2p core level spectrum which consists of spin-orbit doublets and their respective satellites. The Mn $2p_{3/2}$ peak (at 640.68 eV attributed to Mn^{2+} cations and at 642.06 eV attributed to Mn^{3+} cations) has combined satellites, due to this peak being located at 645.75 eV. Furthermore, the peak at 652.96 eV corresponds to Mn $2p_{1/2}$ with its satellite at 657.54 eV. For the Ce 3d core level spectrum (Figure 4.7(d)), the observed peaks at 882.72 eV and 888.47 eV are attributed respectively to Ce^{3+} and Ce^{4+} cations of Ce $3d_{5/2}$. The peak at 901.88 eV correspond to Ce $3d_{3/2}$ with its satellite peak at 916.21 eV. The Fe 2p spectrum shown in Figure 4.7(e) consists of two spin-orbit doublets situated as follows: Fe $2p_{3/2}$ (710.43 eV, Fe^{3+} in B-sites and 712.45 eV, Fe^{3+} in A-sites) with combined shake-up satellites centred at 718.20 eV and Fe $2p_{1/2}$ (724.10 eV, Fe^{3+} in B-sites and 725.61 eV, Fe^{3+} in A-sites) with its satellite centred at 732.32 eV. The oxidation state of Co and Fe (Co^{2+} and Fe^{3+}) in the sample is confirmed by the binding energy of Co 2p and Fe 2p peaks and their satellites. The spectra also indicate the presence of Co and Fe at the octahedral and tetrahedral sites **[20]**. The O 1s spectrum (Figure 4.7(f)) consists of three peaks attributed to lattice oxygen (centred at 529.00 eV), chemisorbed surface oxygen (centred at 529.90 eV) **[17]** and the hydroxyl group (centred at 531.23 eV). Lattice oxygen is inherent in the structure of the sample.

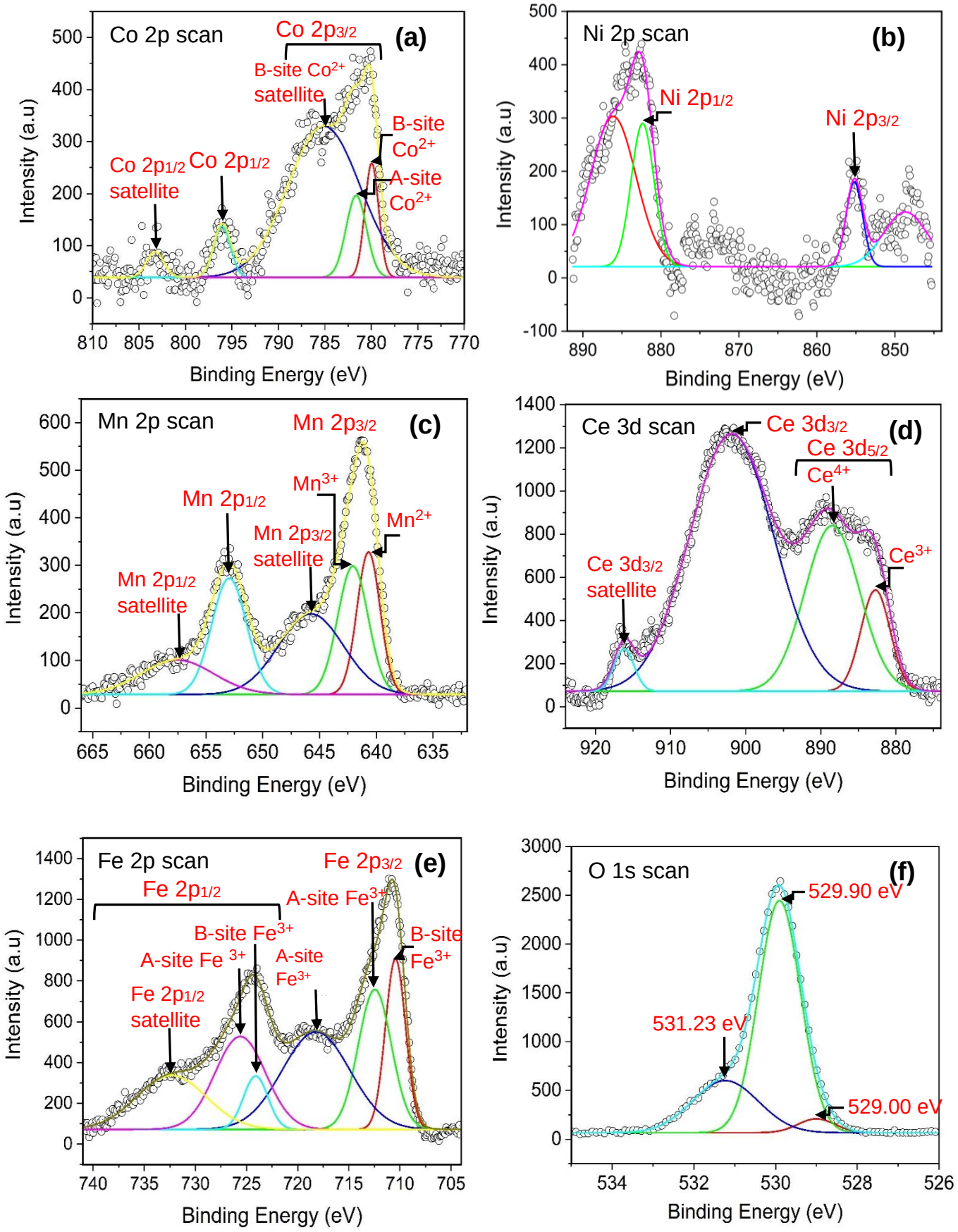

Figure 4.7. XPS spectra of Co1-2xNixMnxFe2-yCeyO4 sample for which x = y = 0.1: (a) Co 2p scan, (b) Ni 2p scan, (c) Mn 2p scan (d) Ce 3d scan, (e) Fe 2p scan, and (f) O 1s scan.

Figures 4.8(a-f) depicts the X-ray photo-electron spectroscopy (XPS) of the $Co_{1-2x}Ni_xMn_xFe_{2-y}Ce_yO_4$ nanoferrite with x = y= 0.2. The Co 2p core level shown in Figure 4.8(a) indicates the presence of Co^{2+} cations (at 780.63 eV) in the B-site of the sample with its satellite at 784.99 eV. The Co $2p_{1/2}$ peak is located at 795.76 eV. The Ni 2p core level spectrum in figure 4.8b is similar to that of figure 4.7(b): there is only a slight difference in the peaks' positions. The Mn 2p, (Figure 4.7(c)), Ce 3d (Figure 4.8(d)), Fe 2p (Figure 4.8(e)), and O 1s (Figure 4.8(f)) core level spectra indicate the successful formation of the spinel. The Ce 3d spectrum (Figure 4.8(d)) suggests there are more Ce^{4+} ions present in the sample than Ce^{3+} ions. The peaks situated at 882.50, 888.20, 898.13, 900.75, 916.54 eV, are assigned to Ce^{4+} ions while the peak located at 902.28 eV is assigned to Ce^{3+} ions. **[15, 21]**.

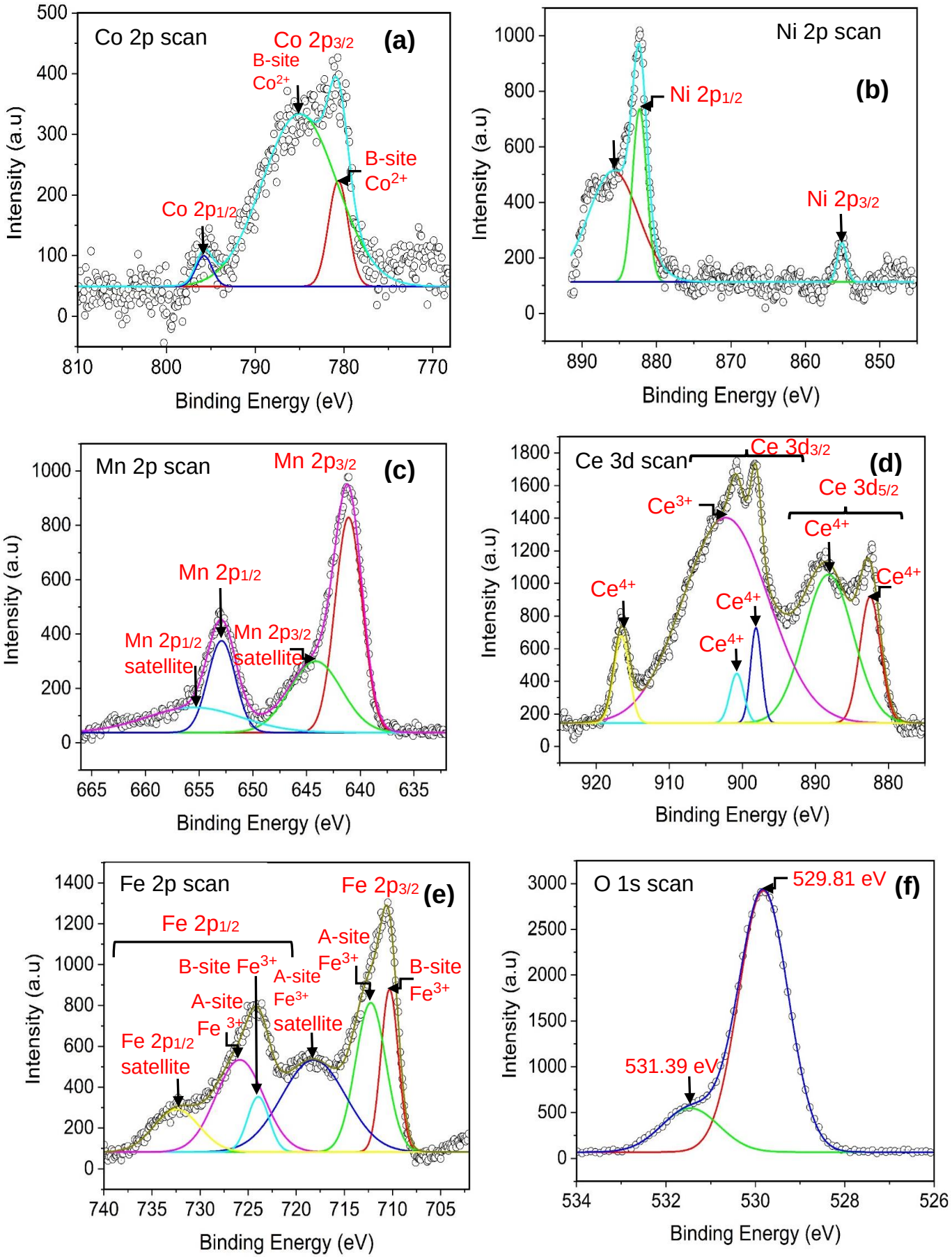

Figure 4.8. XPS spectra of Co1-2xNixMnxFe2-yCeyO4 sample for which x = y = 0.2: (a) Co 2p scan, (b) Ni 2p scan, (c) Mn 2p scan (d) Ce 3d scan, (e) Fe 2p scan, and (f) O 1s scan.

Figures 4.9(a-f) represents the XPS spectra of $Co_{2x}Ni_xMn_xFe_{2-y}Ce_yO_4$ nanoferrite with x = y= 0.3. The core level spectra are almost similar in pattern to that of $Co_{0.6}Ni_{0.2}Mn_{0.2}Ce_{0.2}Fe_{1.8}O_4$ sample. The elements: Co, Ni, Mn, Fe, Ce, O are present in the sample. As expected for an inverse spinel, Co^{2+} cation is present in the B-site (Figure 8(a)). The peak at the lower binding energy (Figure 8(b)) could not be assigned to Ni, taking into account the binding energy position. The core level spectra of Mn, Ce, Fe, and O (Figure 8(c-f)) are somewhat similar to their respective counterparts in Figure 4.7(c-f) with some slight shift in the corresponding peak positions.

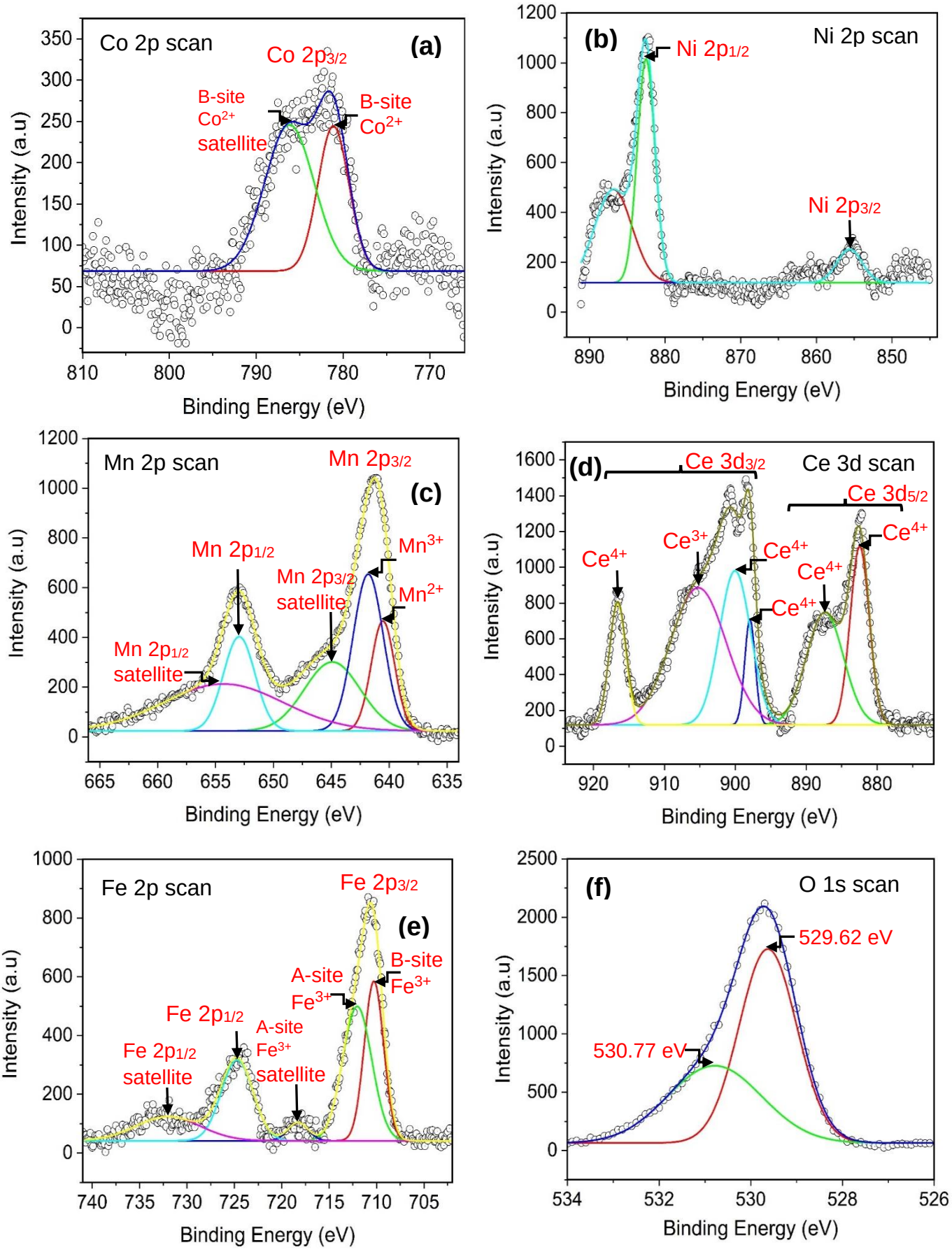

Figure 4.9. XPS spectra of Co1-2xNixMnxFe2-yCeyO4 sample for which x = y = 0.3: (a) Co 2p scan, (b) Ni 2p scan, (c) Mn 2p scan (d) Ce 3d scan, (e) Fe 2p scan, and (f) O 1s scan.

4.3.2. Gas sensing performance of $Co_{1-2x}Ni_xMn_xFe_{2-y}Ce_yO_4$ nanoferrites

The sensors were exposed to flammable and VOC gases (ethanol, propanol, ammonia, and LPG) at an operating temperature of 225 ºC. At the lower operating temperature of 175 ºC, the responses reduced. The concentration range for each of the target gases is based on the recommended exposure limits (Ethanol: 5, 10, 20, 40, 60, 80, and 100 ppm; propanol: 5, 10, 20, 40, 50, 80, 100 ppm; ammonia: 40, 60, 80, 100, 150, 250, 500, 1000 ppm; LPG: 1000 – 10000 ppm). Dry air and helium gases were used, at different times, as carrier gases and for diluting the analyte gases. The best performance of the $CoFe_2O_4$ light-dried sample, using dry air as carrier gas, was towards propanol with the response, response time, and recovery time of 8.13 (toward 100 ppm), 2.35 minutes, and 4.85 minutes respectively. Towards the other gases, the response and recovery times were much longer, although the responses toward ethanol and LPG were close to 8.13. In helium gas atmosphere, this sensor was more sensitive to ethanol than other analyte gases. The response is 20 (toward 100 ppm), with response and recovery times of 8.50 minutes and 7.35 minutes respectively. The response of this sample was 12.33 to 6000 ppm of LPG. This was next to the best response, with relatively short response and recovery times (2.85 min and 4.85 min). However, the response began to reduce from 7000 ppm due to the fluctuation in operating temperature characterising LPG sensing. Towards 100 ppm concentration of propanol, the response was about 9 with almost as long response and recovery times as with ethanol. In dry air atmosphere, the sensor based on the naturally dried $CoFe_2O_4$ sample, had a response of 9.01 towards 1000 ppm of ammonia. The response and recovery times were 5.25 minutes and 3.17 minutes respectively. Its response to ethanol, propanol, and LPG were respectively, 5.39, 6.45 and 3.91. The response and recovery times were in the order of hundreds of seconds, except the

response time towards LPG which was 1.35 minutes. This sample, in helium gas atmosphere, had a response of 8.39 towards 6000 ppm of LPG, with the response and recovery times of 3.48 minutes and 3.77 minutes respectively. The response toward ammonia decreased consecutively from the very first concentration instead of increasing. The response to ethanol and propanol was as good as to LPG although with the longer response and recovery times. In dry air atmosphere, the doped samples ($Co_{0.8}Ni_{0.1}Mn_{0.1}Fe_{1.9}Ce_{0.1}O_4$, $Co_{0.6}Ni_{0.2}Mn_{0.2}Fe_{1.8}Ce_{0.2}O_4$, and $Co_{0.4}Ni_{0.3}Mn_{0.3}Fe_{1.7}Ce_{0.3}O_4$ spinel ferrites) experienced charge carrier transition from n to p-type upon LPG sensing. This transition began partly at 4000 ppm concentration, affecting their response toward LPG. However, in helium gas atmosphere the pattern was completely different. While no charge carrier transition occurred, the response began to diminish from 7000 ppm concentration upward, making the highest response to the LPG to occur at 6000 ppm concentration. This occurrence could be the result of series of fluctuations in sensor current accompanying LPG sensing in helium ambient. Unlike in LPG sensing in dry air atmosphere, these fluctuations not only occurred during sensor/gas interaction but also when the sensor was expected to undergo relaxation before gas-in for the subsequent concentration cycle. An in-depth study of this strange phenomenon may be necessary for the future for an adequate understanding. Another interesting observation is the high response (116.43) recorded towards LPG (6000 ppm) in helium gas atmosphere on the $Co_{0.8}Ni_{0.1}Mn_{0.1}Fe_{1.9}Ce_{0.1}O_4$ sample. Moreover, the overall performance of the sensors in helium gas atmosphere indicates the sensor's seeming preference for operation in an oxygen-deficient atmosphere, and its selectivity toward LPG.

The 3D selectivity plot of $Co_{0.8}Ni_{0.1}Mn_{0.1}Fe_{1.9}Ce_{0.1}O_4$ spinel nanoferrite is depicted in figure 4.9. Samples S1, S2, S3, S4, and S5 are $CoFe_2O_4$ lamp-dried, $CoFe_2O_4$ natural-

dried, $Co_{0.8}Ni_{0.1}Mn_{0.1}Fe_{1.9}Ce_{0.1}O_4$, $Co_{0.6}Ni_{0.2}Mn_{0.2}Fe_{1.8}Ce_{0.2}O_4$, and $Co_{0.4}Ni_{0.3}Mn_{0.3}Fe_{1.7}Ce_{0.3}O_4$ spinel nanoferrites respectively. It is clear from the 3D plot that the $Co_{0.8}Ni_{0.1}Mn_{0.1}Fe_{1.9}Ce_{0.1}O_{4-}$ based sensor was selective to LPG in helium gas atmosphere, with the high response of 116.43, response time of 2.68 minutes, and recovery time of 3.01 minutes, whereas when the same sensor was exposed to LPG in dry air atmosphere, the response was very low. In addition, there was a transition in charge carrier from n to p-type which began at the 4000 ppm concentration of LPG. However, this sensor and others behaved abnormally upon LPG detection. The response increased from 1000 ppm to 6000 ppm then decreased the same way from 7000 ppm to 10000 ppm. This made the response at 10000 ppm (81.73) to be less than the response towards 6000 ppm. It is possible that the response would have been much greater than 116.43 had the abnormal response decrease not occurred.

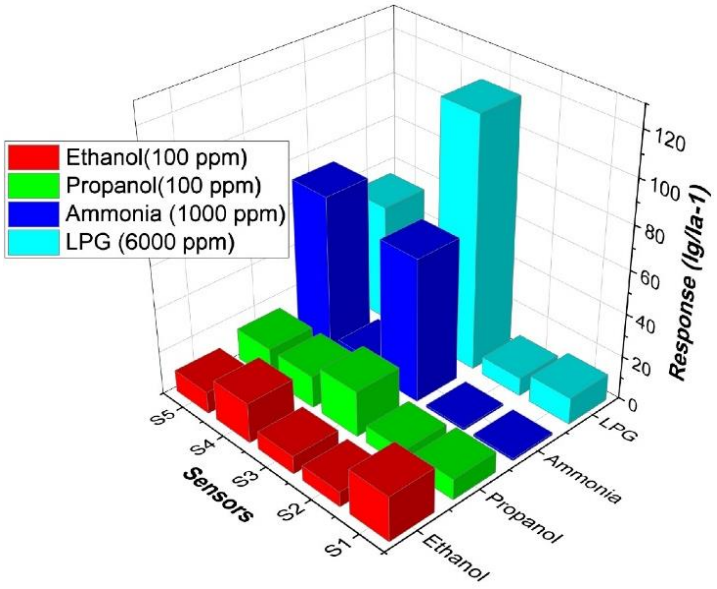

Figure 4.10. 3D selectivity plot showing the gas sensing performance of Co0.8Ni0.1Mn0.1Fe1.9Ce0.1O4 spinel nanoferrite in helium gas atmosphere.

The sensor had a response of 66.57 towards 1000 ppm concentration of ammonia. The $Co_{0.4}Ni_{0.3}Mn_{0.3}Fe_{1.7}Ce_{0.3}O_4$-based sensor also had a response of 72.56 towards 1000 ppm concentration of ammonia under the same operating conditions.

Furthermore, while the sensors' response pattern towards other gases was normal, it was generally abnormal towards LPG (and occasionally, towards NH_3) irrespective of the carrier gas. The abnormal sensitivity pattern of the sensors toward LPG is portrayed in figure 4.11 for dry air atmosphere and in figure 4.12 for helium gas atmosphere.

Table 4.2 describes the symbols denoting response to LPG concentrations presented in figures (4.11-4.12). The green arrows in figure (4.11-4.12) signify the moment LPG was allowed into the chamber and began to react with the sensing surface. The red arrows indicate the time the gas supply into the chamber was cut off. It is clear from figure 4.11(a) that an abnormal oscillation in sensor current began to occur at 3000 ppm LPG concentration and became very prominent at 6000 ppm concentration. In the natural-dried $CoFe_2O_4$ sample (Figure 4.10(b)), the oscillation started from 4000 ppm LPG concentration and continued until 10000 ppm.

Table 4.2. Description of the symbols for LPG concentrations presented in figure (10-11).

Symbol	ppm
1k	1000
2k	2000
3k	3000
4k	4000
5k	5000
6k	6000
7k	7000
8k	8000
9k	9000
10k	10000

On the doped samples, the anomaly is vividly distinguished, as there was not only current oscillation but also the majority charge carrier transition from n- to p-type. Whereas the last 7 cycles of gas concentration (Figure 4.11(c)) show p-type charge

carrier characteristics preceded by the abnormal current oscillation at 3000 ppm. Figure 4.11(a-e) shows**,** LPG sensing performance of the samples in dry air atmosphere (i.e., as carrier gas for the target gas). It is observed from figure 4.11(c) that LPG sensing of the $Co_{0.8}Ni_{0.1}Mn_{0.1}Fe_{1.9}Ce_{0.1}O_4$ sample was accompanied by two distinct phenomena– abnormal current oscillation and majority charge carrier transition. The other two doped samples, $Co_{0.6}Ni_{0.2}Mn_{0.2}Fe_{1.8}Ce_{0.2}O_4$ and $Co_{0.4}Ni_{0.3}Mn_{0.3}Fe_{1.7}Ce_{0.3}O_4$ (figure 4.11(d-e)) followed the same pattern on LPG detection- the first 3 cycles show n-type characteristics while the last 7 cycles show p-type characteristics. The effect of double substitution on cobalt ferrite is evident in the charge carrier transition that occurred on the doped samples only, which never occurred on the undoped cobalt ferrite.

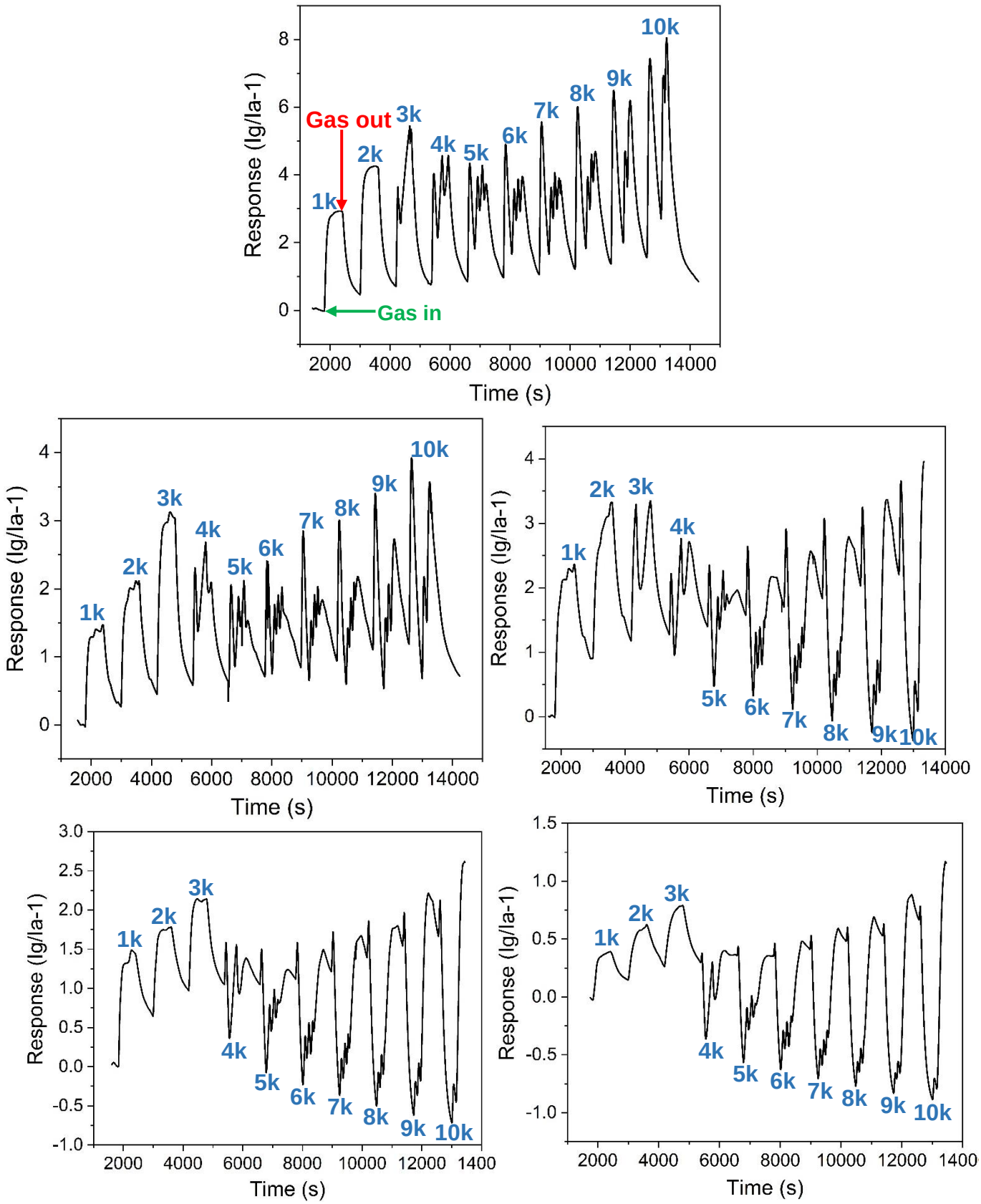

Figure 4.11. Sensitivity plot of (a) CoFe2O4 lamp-dried, (b) CoFe2O4 natural-dried, (c) Co0.8Ni0.1Mn0.1Fe1.9Ce0.1O4, (d) Co0.6Ni0.2Mn0.2Fe1.8Ce0.2O4, and (e) Co0.4Ni0.3Mn0.3Fe1.7Ce0.3O4 towards LPG diluted with dry air atmosphere.

In figure 4.12**,** the LPG sensing performance of the samples in helium gas atmosphere (i.e., helium gas as a carrier gas) is exhibited. The response pattern is the same throughout the samples. In this case, two distinct features characterise the gas sensing activity. The first is the abnormal current oscillation during the sensors' operation and relaxation; the second is the decrease in sensor response after the 6000 ppm concentration. These clearly distinguish it from the sensors' operation in dry air atmosphere (Figure 4.11). The oscillation in current, especially during LPG sensing in dry air, appears to have been triggered by the fluctuation of the operating temperature.

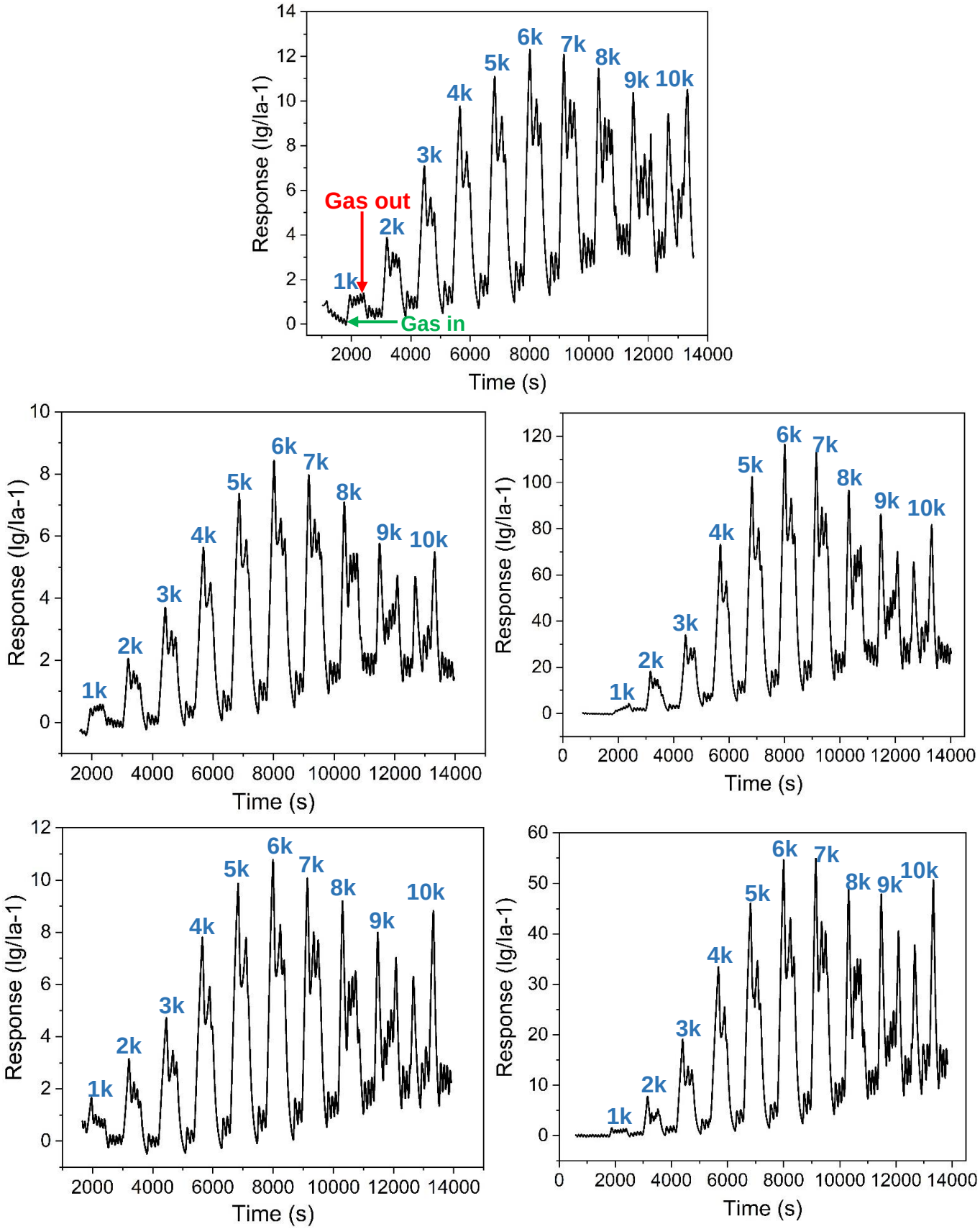

Figure 4.12. Sensitivity plot of (a) CoFe2O4 lamp-dried, (b) CoFe2O4 natural-dried, (c) Co0.8Ni0.1Mn0.1Fe1.9Ce0.1O4, (d)Co0.6Ni0.2Mn0.2Fe1.8Ce0.2O4, and (e) Co0.4Ni0.3Mn0.3Fe1.7Ce0.3O4 towards LPG diluted with helium gas atmosphere

Figure 4.13 demonstrates the connection between this oscillating current and the operating temperature. t_{op} and t_c are the times the operating temperature began fluctuating and the time sensor current started oscillating, respectively. It was found that t_{op}= 5424 s, and t_c = 5384 s, implying the fluctuation in the operating temperature was preceded by current oscillation, which started 40 seconds earlier, whereas it could be suggested that the former preceded the latter based on observation. The cause of this anomaly is still not clearly understood. However, it appears to depend largely on two factors, namely, the operating temperature and the gas concentration. Operating the sensors at lower temperatures (175 °C) or testing lower LPG concentrations was observed to cause a delay in the occurrence of this anomaly. However, it may not be valid to say that the anomaly will never occur at a certain LPG concentration or sensor's operating temperature. Figure 4.13(b) shows the response of the sensors at 225 °C toward 6000 ppm of LPG using helium as carrier gas. The outstanding response of $Co_{0.8}Ni_{0.1}Mn_{0.1}Fe_{1.9}Ce_{0.1}O_4$ sample towards LPG in an oxygen-deficient chamber is noteworthy. This sample was further tested under nitrogen and argon gas atmosphere, and the result is summarised in table 4.3. While the sample was not sensitive in the argon gas atmosphere, interestingly, the undoped naturally dried cobalt ferrite was. The $Co_{0.8}Ni_{0.1}Mn_{0.1}Fe_{1.9}Ce_{0.1}O_4$-based sensor retained about 65% of its initial performance within a period of 10 months.

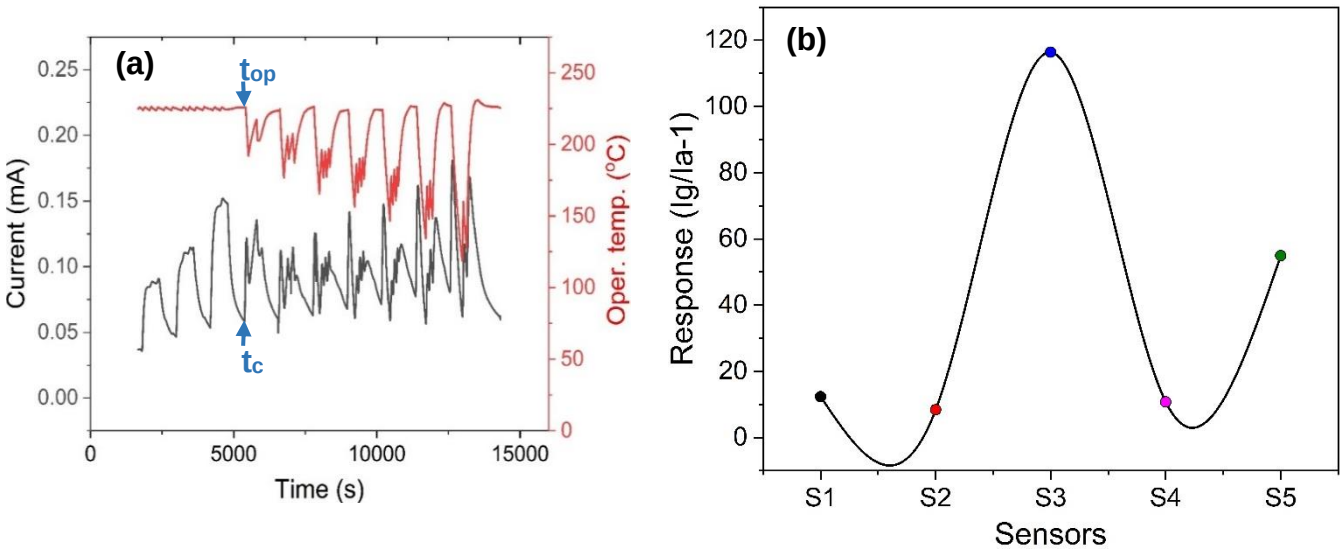

Figure 4.13. (a) dependence of current oscillation on fluctuating operating temperature in natural-dried CoFe2O4 sample (b) 6k ppm LPG sensing response of the sensors in helium gas atmosphere.

Table 4.3. Performance of $Co_{0.8}Ni_{0.1}Mn_{0.1}Fe_{1.9}Ce_{0.1}O_4$ sample towards LPG in various carrier gases.

Carrier gas	Dry air	Nitrogen	Helium	Argon
Response	5.87	5.28	116.43	X
Res. time(min)	5.83	5.83	2.68	X
Rec. time(min)	4.00	4.28	3.01	X

References

[1]. P. Munindra, M. Reddy, B. Rani, N. Jayarambabu, S. Kailasa, P. Rao, K. Rao. A high-performance low-temperature LPG detection by $MgFe_2O_4/BiVO_4$ chemiresistive sensor. Journal of Materials Science: Materials in Electronics 31 (2020) 2370–2377.

[2]. M. Almessiere, Y. Slimani, S. Ali, A. Baykal, I. Ercan, H. Sozeri. Nd^{3+} Ion-Substituted $Co_{1-2x}Ni_xMn_xFe_{2-y}Nd_yO_4$ Nanoparticles: Structural, Morphological, and Magnetic Investigations. Journal of Inorganic and Organometallic Polymers and Materials 29 (2019) 783–791.

[3]. M. Almessiere, Y. Slimani, S. Güner, M. Nawaz, A. Baykal, F. Aldakheel, S. Akhtar, I. Ercan, I. Beleli, B. Ozçelik. magnetic and structural characterization of Nb^{3+} -substituted $CoFe_2O_4$ nanoparticles. Journal of Ceramics International 45 (2019) 8222-8232.

[4]. M. Almessiere, Y. Slimani, A. Baykal. Synthesis and characterization of $Co_{1-2x}Ni_xMn_xFe_{2-y}Ce_yO_4$ nanoparticles. Journal of Rare Earths 38 (2020) 188-194.

[5]. B. Rani, M. Ravina, B. Saravanakumar, G. Ravi, V. Ganesh, S. Ravichandran, R. Yuvakkumar. Ferrimagnetism in cobalt ferrite ($CoFe_2O_4$) nanoparticles. Journal of Nano-structures and Nano-objects 14 (2018) 84-91.

[6]. D. Motaung, Z. Tshabalala, P. Makgwane, F. Mahmoud, D. Oosthuizeni, F. Cummings, N Leshabane, N. Hintsho-Mbita, X. Li, S. Ray, H. Swart. Multi-Functioning of CeO_2-SnO_2 Heterostructure as Room Temperature Ferromagnetism and Chemiresistive Sensors, Journal of Alloys and Compounds, 901 (2022) 164317.

[7]. V. Kirankumar. N. Mayank, S. Sumathi. Photocatalytic performance of cerium doped copper aluminate nanoparticles under visible light irradiation. Journal of the Taiwan Institute of Chemical Engineers 95 (2019) 602-615.

[8]. I. Nurhasanah, W. Safitri, Z. Arifin, A. Subagio, T. Windarti. Antioxidant activities and dose enhancement factor of CeO_2 nanoparticles synthesized by precipitation method. Institute of Physics Conference Series, Journal of Materials Science and Engineering 432 (2018) 012031.

[9]. P. Mkwae, S. Ogundipe, M. Jozela, N. Revaprasadu, S. Nkosi. The heat rate kinetics on the liquefied hydrocarbon gases sensing and food quality control detecting strategy. Journal of Materials Chemistry and Physics 277 (2022) 125550.

[10]. N. Chandamma, S. Kumar, G. Shankarmurthy, E. Melagiriyappa, K. Nagaraja. Effect of gamma irradiation on some electrical and dielectric properties of Ce^{3+} substituted Ni-Zn nano ferrites. Chinese Journal of Physics 55 (2017) 1729-1738.

[11]. J. Wang, A. Sun, Y. Jiang. Structural and magnetic properties of Ce^{3+} doped Mg-Co ferrite prepared by sol–gel method. Journal of Material Science: Material Electronics 33 (2022) 11881-11895.

[12]. L. Li, X. Zhong, R. Wang, X. Tu, L. He, F. Wang. Effects of Ce substitution on structural and electromagnetic properties of NiZn nano ferrite. Journal of Magnetism and Magnetic Materials 475 (2019) 1-4.

[13]. R. Hailstone, A. DiFrancesco, J. Leong, T. Allston, K. Reed. A study of lattice expansion in CeO_2 nanoparticles by transmission electron microscopy. Journal of Physical Chemistry C 113 (2009) 15155-15159.

[14]. M. Nemufulwi, H. Swart, G. Mhlongo. A comprehensive comparison study on magnetic behaviour, defects-related emission and Ni substitution to clarify the origin of enhanced acetone detection capabilities. Journal of Sensors and Actuators: B. Chemical 339 (2021) 129860.

[15]. K. Kim, J. Seo, M. Lee, J. Moon, K. Lee, D. K. Yi, U. Paik. Ce^{3+}-enriched core–shell ceria nanoparticles for silicate adsorption. Journal of Material Research Society 32 (2017) 14.

[16]. H. Wu, T. Yang, Y. Du, L. Shen, G. Ho. Identification of Facet-Governing Reactivity in Hematite for Oxygen Evolution. Journal of Advanced Materials 30 (2018) 1804341.

[17]. F. He, J. Chen, S. Liu, Z. Huang, G. wei, G. Wang, Y. Cao, K. Zhao. $La_{1-x}Sr_xFeO_3$ perovskite-type oxides for chemical-looping steam methane reforming: Identification of the surface elements and redox cyclic performance. International Journal of Hydrogen Energy 44 (2019) 10265-10276.

[18]. X. Wang, S. Li, L. Xie, X. Li, D. Lin, Z. Zhu. Low-temperature and high sensitivity H_2S gas sensor based on ZnO/CuO composite derived from bimetal metal-organic frameworks. Journal of Ceramics International 46 (2020) 15858-15866.

[19]. T. Alves, B. Amorim, M. Torres, C. Bezerra, S. Medeiros, P. Gastelois, L. Outon, W. Macedo**.** Wasp-waisted behavior in magnetic hysteresis curves of CoFe2O4 nanopowder at a low temperature: experimental evidence and theoretical approach. Royal Society of Chemistry Advances 7 (2017) 22187.

[20]. M. Almessiere, Y. Slimani, A. Baykal. Synthesis and characterization of $Co_{1-2x}Ni_xMn_xFe_{2-y}Ce_yO_4$ nanoparticles. Journal of Rare Earths 38 (2020) 188-194.

[21]. K. Maslakov, Y. Teterin, A. Popel, A. Teterin, K. Ivanov, S. Kalmykov, V. Petrov, P. Petrov, I. Farnan. XPS study of ion irradiated and unirradiated CeO_2 bulk and thin film samples. Journal of Applied Surface Science 448 (2018) 154-162.

CHAPTER 5

5. CONCLUSION AND RECOMMENDATION

The casualties and loss of property resulting from the explosion of liquefied petroleum gas (LPG) calls for a very efficient means of detecting and monitoring it. Chemical gas sensors have been widely investigated for LPG sensing. Some important requirements, however, in an efficient LPG sensor include lower operating temperature, speed, stability, selectivity, humidity resistance and applicability in an oxygen-deficient environment.

In this work, the $Co_{1-2x}Ni_xMn_xFe_{2-y}Ce_yO_4$ double-substitution spinel was investigated for sensing performance towards LPG. The samples: $CoFe_2O_4$ (dried with infrared lamp), $CoFe_2O_4$ (dried naturally) and the other three samples ($Co_{0.8}Ni_{0.1}Mn_{0.1}Fe_{1.9}Ce_{0.1}O_4$, $Co_{0.6}Ni_{0.2}Mn_{0.2}Fe_{1.8}Ce_{0.2}O_4$, and $Co_{0.4}Ni_{0.3}Mn_{0.3}Fe_{1.7}Ce_{0.3}O_4$) which are the product of appropriate substitution were synthesised via the glycolthermal route using: $CoCl_2.6H_2O$ (97 %), $NiCl_2.6H_2O$ (98 %), $MnCl_2.4H_2O$ (99 %), $CeCl_3.7H_2O$ (99.9 %) and $FeCl_3.6H_2O$ (98 %) as starting materials, distilled water as solvent for dissolving the chlorides, ammonium hydroxide as precipitant, and ethylene glycol as liquid for the reaction. The products were dried and annealed to obtain the powder samples. The powder samples went through a number of characterisation techniques to study certain properties of the materials. X-ray diffraction (XRD) analysis confirmed the cubic spinel formation and the crystallinity of the samples, as well as giving crystallite sizes information. The surface morphology of each sample was studied by scanning electron microscopy (SEM) which revealed that the samples are agglomerated in different proportions. High resolution transmission electron micrographs (HRTEM) support the XRD results by further confirming the spinel formation and the samples' crystallinity- which is indicated by the brightness of

the rings. The X-ray photoelectron spectroscopy (XPS) shows the elements present in each of the samples. Brunauer-Emmett-Teller (BET) surface area analysis was conducted to ascertain the specific surface area and porosity of the powder samples. Afterwards, the sensors were fabricated by drop-casting each sample dispersed in ethanol and sonicated, onto gold-screen printed alumina substrate to form a thin sensing layer on the substrate. The fabricated sensors were then placed simultaneously in the gas testing chamber for interaction with target gases. The data obtained was properly analysed to obtain the sensor's response, response time, recovery time and other useful information regarding the sensing performance of the sensors.

The sensors were operated at 225 °C and allowed to interact with ethanol, propanol, ammonia (NH_3) and liquefied petroleum gas (LPG), first with dry air as the carrier gas (dry air atmosphere) and then later with helium as carrier gas (helium gas atmosphere). The sensors' performance in dry air atmosphere was not very impressive. The best response was 9 towards 1000 ppm of ammonia on $CoFe_2O_4$ (natural-dried) sample. The response towards 100 ppm of ethanol lies between 1 and 7. Toward 100 ppm of propanol, the response ranged from 1 to about 8, whereas LPG sensing was characterised by charge carrier transition from n- to p-type. This transition began to occur at 4000 ppm of LPG, while the first three cycles were normal n-type material characteristic. The response and recovery times were also relatively long. In view of this, the double-substitution spinel might not be efficient enough, on its own, for LPG sensing in an oxygen-dominant environment. However, the sensors displayed excellent performance in helium gas atmosphere, especially the $Co_{0.8}Ni_{0.1}Mn_{0.1}Fe_{1.9}Ce_{0.1}O_4$ sensor which had a response of 116.43 towards 10000 ppm of LPG and the $Co_{0.4}Ni_{0.3}Mn_{0.3}Fe_{1.7}Ce_{0.3}O_4$ sensor with a response of 72.56

toward 1000 ppm of NH_3, and with relatively short response and recovery times. This kind of device could be a potential tool for LPG detection in an oxygen-deficient environment, although enhancement would be needed to improve its gas response in an oxygen-dominant atmosphere. When nitrogen was used as carrier gas (nitrogen-dominant ambient) for LPG, the $Co_{0.8}Ni_{0.1}Mn_{0.1}Fe_{1.9}Ce_{0.1}O_4$-based sensor showed small response as in the case of dry air atmosphere. This sensor did not respond well towards LPG in argon-dominant environment. This raised a crucial question for consideration: helium and argon gases are both inert, but why the sensitivity in one and not in the other? In spite of the anomalous fluctuation in current associated with LPG sensing characteristics of this sensor, it was found to exhibit high stability within a period of 10 months. The sensor, though operates at high temperature and senses with accompanying current oscillation, exhibits suitable characteristics for applicability in LPG detection and monitoring.

It has been established that, operating temperature and gas concentration play a key role in the abnormal occurrence of the fluctuation of the operating temperature and current oscillation while the sensors operate in dry air atmosphere. In addition, as the sensors operate in helium-dominant atmosphere, the current oscillation was observed at the peak as well as at relaxation regardless of the gas under test. However, more vivid understanding of this abnormal phenomenon will be required to fabricate efficient sensor for monitoring liquefied petroleum gas in order to mitigate the risk associated with the use of the gas. Therefore, such questions as follows might be very useful for more extensive study of this anomaly:

i. What would be the effect on gas sensing if synthesis method or condition of the sensor materials were changed?

ii. Could this same anomaly occur if different sensor materials were subjected to investigation?

iii. How can the temperature fluctuation be effectively controlled during LPG sensing activity of this material?

LIST OF REFERENCES

[1]. R. Serway, J. Jewett. Physics for scientist and engineers with modern physics 9 (2014) 417.

[2]. L. Zhu, W. Zeng. Room temperature gas sensing of ZnO-based gas sensor: A review. Journal of Sensors and Actuators A 267 (2017) 242-261.

[3]. H. Ji, W. Zeng, Y. Li. Gas sensing mechanism of metal oxide semiconductors: A focus review. Journal of Nanoscale 11 (2019) 22664-22684.

[4]. M. Nemufulwi, H. Swart, G. Mhlongo. A comprehensive comparison study on magnetic behaviour, defects-related emission and Ni substitution to clarify the origin of enhanced acetone detection capabilities. Journal of Sensors and Actuators: B. Chemical 339 (2021) 129860.

[5]. G. Manjunath, S. Pujaria, D. Patil, S. Mandala. A scalable screen-printed performance ZnO-UV and Gas Sensor: Effect of solution combustion. Journal of Materials Science in Semiconductor Processing 107 (2020) 104828.

[6]. M. Singh, B. Yadav, A. Ranjan, R. Sonker, M. Kaur. Detection of liquefied petroleum gas below lowest explosion limit (LEL) using nanostructured hexagonal strontium ferrite thin film. Journal of Sensors and Actuators B 249 (2017) 96 – 104.

[7]. S. Bagga, J. Akhtar, S. Mishra, Preeti. Fabrication of coplanar microheater platform for LPG sensing application. Springer Nature 26 (2019) 731-738.

[8]. V. Manikandan, M. Singh, B. Yadav, R. Mane, S. Vigneselvand, A. Mirzaei, J. Chandrasekaran. Room temperature LPG sensing properties of tin substituted copper ferrite (Sn-$CuFe_2O_4$) thin film. Journal of Materials Chemistry and Physics 240 (2020) 122265.

[9]. M. Reddy, S Kailasa· B. Rani· N. Jayarambabu · K. Bikshalu· P. Munindra · K. Rao. MgO@CeO2 chemiresistive fexible sensor for room temperature LPG detection. Journal of Materials Science 30 (2019) 17295–17302.

[10]. P. Munindra, M. Reddy, B. Rani, N. Jayarambabu, S. Kailasa, P. Rao, K. Rao. A high-performance low-temperature LPG detection by MgFe2O4/BiVO4 chemiresistive sensor. Journal of Materials Science: Materials in Electronics 31 (2020) 2370-2377.

[11]. G. Korotcenkov. Handbook of Gas Sensor Materials: Properties, Advantages and Shortcomings for Application: New Trends and Technologies, Integrated Analytical Systems 1 (2014) 167-195.

[12]. G. Neri. First fifty years of chemoresistive gas sensors. Journal of Chemosensors 3 (2015) 1-20.

[13]. H. Nazemi, A. Joseph, J. Park, A. Emadi. Advanced micro- and nano-gas sensor technology: A review. Journal of Sensors 19 (2019) 1285.

[14]. M. Fleischer, M. Lehmann. Solid state gas sensors- Industrial application: Springer series on chemical sensors and biosensors 11 (2012) 53-78.

[15]. C. Kohl, T. Wagner. Gas sensing fundamentals: Springer series on chemical sensors and biosensors 15 (2014) 279-310.

[16]. S. Zhao, W. Ran, D. Wang, R. Yin, Y. Yan, K.Jiang, Z. Lou, G. Shen. 3D dielectric layer enabled highly sensitive capacitive pressure sensors for wearable electronics. Journal of Applied Materials Interfaces 28 (2020) 32023-32030.

[17]. G. Sberveglieri. Gas Sensors: principles, operation, developments. Springer 1 (1992) 329-364.

[18]. P. Karnati, S. Akbar, P. Morris. Conduction mechanisms in one dimensional core-shell nanostructures for gas sensing: A review. Journal of Sensors and Actuators: B. Chemical 295 (2019) 127-143.

[19]. Z. Yuan, R. Li, F. Meng, J. Zhang, K. Zuo, E. Han. Approaches to Enhancing Gas Sensing Properties: A Review. Journal of Sensors 19 (2019) 1495.

[20]. Y. Wong, B. Ang, A. Haseeb, A. Baharuddin, Y. Wong. Conducting Polymers as Chemiresistive Gas Sensing Materials: A Review. Journal of The Electrochemical Society, 167 (2020) 037503.

[21]. A. Mugutka, S. Gore, R. Mane, S. Patang, S. Jadhav, S. Shaikh, A. Al-Enizi, A. Nafady, B. Thamer, M. Ubaidullah. Structural modifications in Co-Zn nanoferrites by Gd substitution triggering to dielectric and gas sensing applications. Journal of Alloys and Compounds 844 (2020) 156178.

[22]. M. Hashim, M. Raghashuda, S. Meena, J. Shah, S. Shirsath, S. Kumar, D. Ravinder, P. Bhatt, Alimuddin, R. kumar, R. Kotnala. Influence of rare earth ion doping (Ce and Dy) on electrical and magnetic properties of cobalt ferrite. Journal of Magnetism and Magnetic Materials 449 (2018) 319-327.

[23]. D. Miller, S. Akbar, P. Morris. Nanoscale metal oxidebased heterojunctions for gas sensing: A review. Journal of Sensors and Actuators B 204 (2014) 250-272.

[24]. A. Dral, J. Elshof. 2D metal oxide nanoflakes for sensing applications: Review and perspective. Journal of Sensors and Actuators: B. Chemical 272 (2018) 369-392.

[25]. Z. Li, H. Li, Z. Wu, M. Wang, J. Luo, H. Torun, P. Hu, C. Yang, M. Grundmann, X. Liud, Y. Fu. Advances in designs and mechanisms of semiconducting metal oxide nanostructures for high-precision gas sensors operated at room temperature. Journal of Materials Horizons 6 (2019) 470.

[26]. Y. Ding, X. Guo, B. Du, X. Hu, X. Yang, Y. He, Y. Zhou, Z. Zang. Low-operating temperature ammonia sensor based on Cu_2O nanoparticles decorated with p-type MoS_2 nanosheets. Journal of Materials Chemistry C 9 (2021) 4838-4846.

[27]. Y. Gautam, K. Sharma, S. Tyagi, A. Ambedkar, M. Chaudhary, B. Singh. Nanostructured metal oxide semiconductor-based sensors for greenhouse gas detection: progress and challenges. Journal of Royal Society Open Science 8 (2021) 201324.

[28]. Z. Anajafi, M. Naseri, G. Neria. Gas sensing and electrochemical properties of rare earth ferrite $LnFeO_3$ (Nd, Sm). Journal of Ceramics International 46 (2020) 26682-26688.

[29]. J. Patil, D. Nadargi, I. Mulla, S. Suryavanshi. Spinel $MgFe_2O_4$ thick films: A colloidal approach for developing gas sensors. Journal of Materials Letters 213 (2018) 27-30.

[30]. P. Koli, K. Kapadnis, U. Deshpandhe. Nanocrystalline-modified nickel ferrite films: an effective sensor for industrial and environmental gas pollutant detection. Journal of nanostructure in chemistry 9 (2019) 95-110.

[31]. T. Roman, D. Gherca, A. Borhan, M. Grigoas, G. Stoian, N. Lupu, I. Turcan, N. Cimpoesu, B. Istrate, I. Radu, R. Danila, A. Pui. Nanostructured quaternary $Ni_{1-x}Cu_xFe_{2-y}Ce_yO_4$ complex system: Cerium content and copper substitution dependence of cation distribution and magnetic-electric properties in spine ferrites. Journal of Ceramic International 47 (2021) 18177-18187.

[32]. A. Rane, K. kanny, V. Abitha, S. Thomas. Methods for synthesis of nanoparticles and fabrication of nanocomposites. Journal of Synthesis of inorganic materials: Advances and key technologies, Micro and Nano Technologies 5 (2018) 121-139.

[33]. V. Chikan, E. McLaurin. Rapid nanoparticle synthesis by magnetic and microwave heating. Journal of Nanomaterials 6 (2016) 85.

[34]. N. Tabrizi, M. Ullmann, V. Vons, U. Lafont, A. Schmidt-Ott. Generation of nanoparticles by spark discharge. Journal of Nanoparticles Research 11 (2009) 315–332.

[35]. H. Zeng, X. Du, S. Singh, S. Kulinich, S. Yang, J. He, W. Cai. Nanomaterials via Laser Ablation/Irradiation in Liquid: A Review. Journal of Advance Functional Materials 22 (2012) 1333–1353.

[36]. A. Varma, A. Mukasyan, A. Rogachev, K. Manukyan. Solution Combustion Synthesis of Nanoscale Materials. Journal of Chemical Reviews 116 (2016) 14493−14586.

[37]. A. Phuruangrat, S. Thongtem, T. Thongtem. Glycolthermal synthesis and characterization of hexagonal CdS round microparticles in flower-like clusters. Journal of Alloys and Compounds 509 (2011) 10150-10154.

[38]. Y. Zou, H. Wang, R. Yang, X. Lai, J. Wan, G. Lin, D. Liu. Controlled synthesis and enhanced toluene-sensing properties of mesoporous $NiCo_{1-x}Fe_2O_4$ nanostructured microspheres with tunable composite. Journal of Sensors and Actuators: B. chemical 280 (2019) 227-234.

[39]. S. Mutkule, S. Nayale, V. Jadhav, S. Ambade, M. Naushad, A. Sagar, V. Patil, F. Standler, R. Mane. Solution-processed nickel oxide films and their liquefied petroleum gas sensing activity. Journal of Alloys and Compounds 689 (2017) 2008-2015.

[40]. P. Shankar, J. Rayappan. Gas sensing mechanism of metal oxide: The role of ambient atmosphere, type of semiconductor and gases- A review. Journal of Science Letters 4 (2015) 126.

[41]. S. Choudharya, S. Annapoorni, R. Malik. Evolution and growth mechanism of hexagonal ZnO nanorods and their LPG sensing response at low operating temperature. Journal of Sensors and Actuators 293 (2019) 201-214.

[42]. U. Nakate, P. Patil, B. Ghule, Y. Nakate, S. Ekar, Revan C. Ambare, R.S. Mane. Room temperature LPG sensing properties using spray pyrolysis deposited nano-crystalline CdO thin films. Journal of Surfaces and Interfaces 17 (2019) 100339.

[43]. N. Singh, P. Singh, M. Singh, D. Gangopadhyay, S. Singh, P. Tandon. Development of a potential LPG sensor based on a PANI–Co3O4 nanocomposite that functions at room temperature. New Journal of Chemistry 43 (2019) 17340.

[44]. G. Singh, R. C. Singh. Highly sensitive and selective liquefed petroleum gas sensor based on novel ZnO–NiO heterostructures. Journal of Materials Science: Materials in Electronics 30 (2019) 20010-20018.

[45]. R. Sonkera, B. Yadav, V. Gupta, M. Tomar. Fabrication and characterization of ZnO-TiO2-PANI (ZTP) micro/nanoballs for the detection of flammable and toxic gases. Journal of Hazardous Materials 370 (2019) 126-137.

[46]. B. Thomas, S. Deepa, K. Kumar. Influence of surface defects and preferential orientation in nanostructured Ce-doped SnO2 thin films by nebulizer spray deposition for lowering the LPG sensing temperature to 150 °C. Journal of Ionics 25 (2019) 809–826.

[47]. H. Dehkordi, A. Mokhtari, K. Dastafkan, V. Soleimanian. Sol–Gel Spin-Coating Followed by Solvothermal Synthesis of Nanorods-Based ZnO Thin Films: Microstructural, Optical, and Gas Sensing Properties. Journal of Electronic Materials 48 (2019) 2.

[48]. M. Taheri, Z. Feizabadi, S. Jafari, N. Mansour. Fast Response and High Sensitivity of Reduced Graphene Oxide/Gold Nano-hybrid for LPG Sensors at Room Temperature. Journal of Electronic Materials 47 (2018) 12.

[49]. K. Khojiera, F. Teimoorib, S. Zolghadrb, M. Pashazanousi. Fast and low concentration detection of liquefied petroleum gas by Auactivated ZnO sensor. Journal of Materials Research Bulletin 108 (2018) 96-100.

[50]. A. Lokhande, A. Yadav, J. Lee, M. He, S. Patil, V. Lokhande, C. Lokhande, J. Kim. Room temperature liquefied petroleum gas sensing using Cu2SnS3/CdS heterojunction. Journal of Alloys and Compound 709 (2017) 92-103.

[51]. A. Singh, S. Singh, P. Tandona. Fabrication of copper ferrite porous hierarchical nanostructures for an efficient liquefied petroleum gas sensor. Journal of Sensors and Actuators B 244 (2017) 806-814.

[52]. S. Kotresh, Y. Ravikiran, S. Tiwari, S. Kumari. Polyaniline–Cadmium Ferrite Nanostructured Composite for Room-Temperature Liquefied Petroleum Gas Sensing. Journal of Electronic Materials 46 (2017) 8.

[53]. S. Kotresh, Y. Ravikirana, S. Kumari, C. Ramana, K. Batoo. Solution based–spin cast processed LPG sensor at room temperature. Journal of Sensors and Actuators A 263 (2017) 687-692.

[54]. N. Shozi, I. Kortidis, P. Mkwae, N. Chonco, N. Leshabane, M. Jozela, R. Kroon, H. Swart, S. Nkosi. Extremely sensitive and selective flammable liquefied hydrocarbon gas sensing and inter-dependence of fluctuating operating temperature and resistance: Perspective of rare-earth doped cobalt nanoferrites. Journal of Alloys and Compounds 859 (2021) 157846.

[55]. A. Kumar, J. Shen, W. Yang, H. Zhao, P. Sharma, D. Varshney, Q. Li. Impact of Rare Earth Gd3+ Ions on Structural and Magnetic Properties of

Ni0.5Zn0.5Fe2−xGdxO4 Spinel Ferrite: Useful for Advanced Spintronic Technologies. Journal of Superconductivity and Novel Magnetism (2018) 31:1173–1182.

[56]. T. Zhou, S. Cao, R. Zhang, J. Tu, T. Fei, T. Zhang. Effect of cation substitution on the gas sensing performances of ternary spinel MCo2O4 (M= Mn, Ni, and Zn). Journal of applied Materials Interfaces. 11 (2019) 28023-28032.

[57]. Y. Li, Y. Lu, K. Wu, D. Zhang, M. Debliquy, C. Zhang. Microwave-assisted hydrothermal synthesis of copper oxide-based gas-sensitive nanostructures. Journal of Rare Metals 40 (2021)1477–1493.

[58]. M. Kasim, N. Kamarulzaman, R. Rusdil, A. Rahman. Effect of pH on the crystal growth of ZnO nanomaterials and their band gap energies. Journal of Physics: Conference series 1083 (2018) 102043.

[59]. G. Yang, S. Park. Conventional and Microwave Hydrothermal Synthesis and Application of Functional Materials: A Review. Journal of Materials 12 (2019) 1177.

[60]. T. Nhlapo, T. Mokoena, J. Msomi, T. Moyo, T. Mahule, M. Nyathi. Synthesis, Electron Spin Resonance and Photoluminescence properties of Sm3+ ion doped Zn-Mn nanoferrites synthesized by glycol-thermal method. Journal of Molecular Structure 1268 (2022) 133703.

[61]. D. Bryce. NMR crystallography: structure and properties of materials from soli-state nuclear magnetic resonance observables. International Union of Crystallography Journal 4 (2017) 350-359.

[62]. L. Kolahalam, I. Viswanath, B. Diwakar, B. Govindh, V. Reddy, Y. Murthy. Review on nanomaterials: synthesis and applications. Materialstoday: Proceedings 18 (2019) 2182-2190.

[63]. N. parab, J. Barnes, C. Zhao, R. Cunningham, K. Fezzaa, A. Rollett, T. Sun. real time observation of binder jetting printing process using high-speed x-ray imaging. Nature 9 (2019) 2499.

[64]. H. Cheng, C. Lu, J. Liu, Y. Yan, X. Han, H. Jin, Y. Wang, Y. Liu, C. Wu. Synchrotron radiation X-ray powder diffraction techniques applied in hydrogen storage materials- A review. Progress in Natural Science: Materials International 27 (2017) 66-73.

[65]. S. Mourdikoudis, R. Pallares, N. Thanh. Characterization techniques for nanoparticles: comparison and complementarity upon studying nanoparticle properties. Journal of Nanoscale 10 (2018) 12871-12934.

[66]. Y. Deng. Common Phase and Structure Misidentifications in High-Resolution TEM Characterization of Perovskite Materials. Journal of Condensed Matter 1 (2021) 6.

[67]. X. Chen, X. Wang, D. Fang. A review on C1s XPS-spectra for some kinds of carbon materials. Journal of Fullerenes, Nanotubes and Carbon Nanostructures 28 (2020) 1048–1058.

[68]. N. Ural. The significance of scanning electron microscopy(SEM)analysis on the microstructure of improved clay: An overview. Journal of Open Geosciences 13 (2021) 197–218.

[69]. P. Toth. Nanostructure quantification of turbostratic carbon by HRTEM image analysis: State of the art, biases, sensitivity and best practices. Carbon, Elsevier 178 (2021) 688-707.

[70]. M. Naderi. surface area: Progress in filtration and separation, Elsevier (2015) 585-608.

71]. M. Almessiere, Y. Slimani, S. Ali, A. Baykal, I. Ercan, H. Sozeri. Nd^{3+} Ion-Substituted $Co_{1-2x}Ni_xMn_xFe_{2-y}Nd_yO_4$ Nanoparticles: Structural, Morphological, and Magnetic Investigations. Journal of Inorganic and Organometallic Polymers and Materials 29 (2019) 783–791.

[71]. M. Almessiere, Y. Slimani, S. Güner, M. Nawaz, A. Baykal, F. Aldakheel, S. Akhtar, I. Ercan, I. Beleli, B. Ozçelik. magnetic and structural characterization of Nb^{3+} -substituted $CoFe_2O_4$ nanoparticles. Journal of Ceramics International 45 (2019) 8222-8232.

[73]. B. Rani, M. Ravina, B. Saravanakumar, G. Ravi, V. Ganesh, S. Ravichandran, R. Yuvakkumar. Ferrimagnetism in cobalt ferrite ($CoFe_2O_4$) nanoparticles. Journal of Nano-structures and Nano-objects 14 (2018) 84-91.

[74]. D. Motaung, Z. Tshabalala, P. Makgwane, F. Mahmoud, D. Oosthuizeni, F. Cummings, N Leshabane, N. Hintsho-Mbita, X. Li, S. Ray, H. Swart. Multi-Functioning of CeO_2-SnO_2 Heterostructure as Room Temperature Ferromagnetism and Chemiresistive Sensors, Journal of Alloys and Compounds, 901 (2022) 164317.

[75]. V. Kirankumar. N. Mayank, S. Sumathi. Photocatalytic performance of cerium doped copper aluminate nanoparticles under visible light irradiation. Journal of the Taiwan Institute of Chemical Engineers 95 (2019) 602-615.

[76]. I. Nurhasanah, W. Safitri, Z. Arifin, A. Subagio, T. Windarti. Antioxidant activities and dose enhancement factor of CeO_2 nanoparticles synthesized by precipitation method. Institute of Physics Conference Series, Journal of Materials Science and Engineering 432 (2018) 012031.

[77]. P. Mkwae, S. Ogundipe, M. Jozela, N. Revaprasadu, S. Nkosi. The heat rate kinetics on the liquefied hydrocarbon gases sensing and food quality control detecting strategy. Journal of Materials Chemistry and Physics 277 (2022) 125550.

[78]. N. Chandamma, S. Kumar, G. Shankarmurthy, E. Melagiriyappa, K. Nagaraja. Effect of gamma irradiation on some electrical and dielectric properties of Ce^{3+} substituted Ni-Zn nano ferrites. Chinese Journal of Physics 55 (2017) 1729-1738.

[79]. J. Wang, A. Sun, Y. Jiang. Structural and magnetic properties of Ce^{3+} doped Mg-Co ferrite prepared by sol–gel method. Journal of Material Science: Material Electronics 33 (2022) 11881-11895.

[80]. L. Li, X. Zhong, R. Wang, X. Tu, L. He, F. Wang. Effects of Ce substitution on structural and electromagnetic properties of NiZn nano ferrite. Journal of Magnetism and Magnetic Materials 475 (2019) 1-4.

[81]. R. Hailstone, A. DiFrancesco, J. Leong, T. Allston, K. Reed. A study of lattice expansion in CeO_2 nanoparticles by transmission electron microscopy. Journal of Physical Chemistry C 113 (2009) 15155-15159.

[82]. K. Kim, J. Seo, M. Lee, J. Moon, K. Lee, D. K. Yi, U. Paik. Ce^{3+}-enriched core–shell ceria nanoparticles for silicate adsorption. Journal of Material Research Society 32 (2017) 14.

[83]. H. Wu, T. Yang, Y. Du, L. Shen, G. Ho. Identification of Facet-Governing Reactivity in Hematite for Oxygen Evolution. Journal of Advanced Materials 30 (2018) 1804341.

[84]. F. He, J. Chen, S. Liu, Z. Huang, G. wei, G. Wang, Y. Cao, K. Zhao. $La_{1-x}Sr_xFeO_3$ perovskite-type oxides for chemical-looping steam methane reforming: Identification of the surface elements and redox cyclic performance. International Journal of Hydrogen Energy 44 (2019) 10265-10276.

[85]. X. Wang, S. Li, L. Xie, X. Li, D. Lin, Z. Zhu. Low-temperature and high sensitivity H_2S gas sensor based on ZnO/CuO composite derived from bimetal metal-organic frameworks. Journal of Ceramics International 46 (2020) 15858-15866.

[86]. T. Alves, B. Amorim, M. Torres, C. Bezerra, S. Medeiros, P. Gastelois, L. Outon, W. Macedo**.** Wasp-waisted behavior in magnetic hysteresis curves of CoFe2O4 nanopowder at a low temperature: experimental evidence and theoretical approach. Royal Society of Chemistry Advances 7 (2017) 22187.

[87]. M. Almessiere, Y. Slimani, A. Baykal. Synthesis and characterization of $Co_{1-2x}Ni_xMn_xFe_{2-y}Ce_yO_4$ nanoparticles. Journal of Rare Earths 38 (2020) 188-194.

[88]. K. Maslakov, Y. Teterin, A. Popel, A. Teterin, K. Ivanov, S. Kalmykov, V. Petrov, P. Petrov, I. Farnan. XPS study of ion irradiated and unirradiated CeO_2 bulk and thin film samples. Journal of Applied Surface Science 448 (2018) 154-162.